PHYSICAL REVIEW B **85**, 064108 (2012)

Probing grain boundary sink strength at the nanoscale: Energetics and length scales of vacancy and interstitial absorption by grain boundaries in α-Fe

M. A. Tschopp[*]
Center for Advanced Vehicular Systems, Mississippi State University, Mississippi State, Mississippi 39762, USA

K. N. Solanki
School for Engineering of Matter, Transport and Energy Arizona State University, Tempe, Arizona 85287, USA

F. Gao, X. Sun, and M. A. Khaleel
Pacific Northwest National Laboratory, Richland, Washington 99354, USA

M. F. Horstemeyer
Center for Advanced Vehicular Systems, Mississippi State University, Mississippi State, Mississippi 39762, USA

(Received 3 May 2011; revised manuscript received 22 December 2011; published 10 February 2012)

The energetics and length scales associated with the interaction between point defects (vacancies and self-interstitial atoms) and grain boundaries in bcc Fe was explored. Molecular statics simulations were used to generate a grain boundary structure database that contained ≈170 grain boundaries with varying tilt and twist character. Then, vacancy and self-interstitial atom formation energies were calculated at all potential grain boundary sites within 15 Å of the boundary. The present results provide detailed information about the interaction energies of vacancies and self-interstitial atoms with symmetric tilt grain boundaries in iron and the length scales involved with absorption of these point defects by grain boundaries. Both low- and high-angle grain boundaries were effective sinks for point defects, with a few low-Σ grain boundaries (e.g., the $\Sigma3\{112\}$ twin boundary) that have properties different from the rest. The formation energies depend on both the local atomic structure and the distance from the boundary center. Additionally, the effect of grain boundary energy, disorientation angle, and Σ designation on the boundary sink strength was explored; the strongest correlation occurred between the grain boundary energy and the mean point defect formation energies. Based on point defect binding energies, interstitials have ≈80% more grain boundary sites per area and ≈300% greater site strength than vacancies. Last, the absorption length scale of point defects by grain boundaries is over a full lattice unit larger for interstitials than for vacancies (mean of 6–7 Å versus 10–11 Å for vacancies and interstitials, respectively).

DOI: 10.1103/PhysRevB.85.064108 PACS number(s): 61.72.J−, 21.10.Dr, 68.35.Dv, 61.72.Mm

I. INTRODUCTION

Future design of nuclear materials requires structural materials that can withstand extreme environment conditions. Displacement cascades caused by neutrons create lattice point defects (vacancies and interstitials), which can have profound effects on the physical and mechanical properties of these alloys through the creation of defects, defect clusters, defect-impurity complexes, voids, and defect-solute clusters.[1] The ability of materials to handle radiation damage is directly related to their ability to remove point defects through various microstructural sinks and mechanisms.[2] Characterizing the mechanisms by which point defects are produced, diffuse, recombine, and are absorbed by sinks can help both our understanding of radiation damage and can help in quantifying the evolution of the underlying material microstructure. Since many structural materials are polycrystalline in nature, grain boundary interactions with both vacancies *and* interstitials play a vital role in the resulting properties of the polycrystalline material.

Quantifying how point defects interact with defect sinks, such as grain boundaries, is also important for understanding radiation-induced segregation of solute and impurity atoms in metals. This topic is of great importance for reactor performance, as radiation-induced segregation is one of many factors that contributes to irradiation-induced stress corrosion cracking. For instance, during radiation-induced segregation, the flux of solute and impurity elements is highly coupled with the flux of vacancy and interstitials. As vacancies and interstitials tend to diffuse and bind to microstructural sinks (e.g., grain boundaries, free surfaces, defect clusters), solute and impurity atoms are spatially redistributed in the vicinity of these sinks. The net result is an accumulation or a depletion of elements at these defect sinks, which can have deleterious effects on polycrystal properties. There have been a number of experimental studies to characterize and understand the mechanisms of radiation-induced segregation in a number of irradiated metal systems[3–13] as well as computational models. Interestingly, these models have to consider both the evolution of defect and defect clusters as well as their destinations. Hence understanding both the interaction of point defects with grain boundaries and the grain boundary sink strengths may be important for such models.

Point-defect behavior and radiation-induced segregation can also be influenced by the grain boundary character of individual grain boundaries. Grain boundary character refers to the five degrees of freedom associated with the misorientation between the crystallographic orientations of the two adjoining grains. Hence grain boundary character encompasses not only the misorientation angle, but also the grain boundary plane and information pertaining to grain boundary type (e.g., tilt versus twist, symmetric versus asymmetric, low angle versus high

©2012 American Physical Society

angle, Σ value, etc.). Experiments have shown that certain coincidence grain boundaries (e.g., $\Sigma3$ and $\Sigma9$) have sink strengths (pertaining to radiation-induced segregation) that deviate from that in general high-angle grain boundaries.[14] Moreover, other experiments have shown differences between grain boundaries in their ability to annihilate point defects.[15] These results present an interesting opportunity for designing radiation-tolerant materials, i.e., the grain boundary character of polycrystalline materials can be engineered to enhance their beneficial effects while reducing their detrimental effects, as was first proposed by Watanabe.[16] Recent advances in both experimentally measuring the grain boundary character distribution[17–21] and applying grain boundary engineering to various material systems[22] may allow for improved materials design of radiation-tolerant materials through thermomechanical processing. However, while experiments can readily supply information pertaining to changes in macroscopic properties due to grain boundary engineering, it is difficult to experimentally understand the behavior of grain boundary character for individual boundaries. Hence nanoscale simulations that probe how grain boundary character and local atomic structure impacts radiation processes can provide insight into how grain boundary character affects the ability of polycrystalline metals to mitigate radiation.

Electronic structure calculations and atomistic simulations in bicrystalline and nanocrystalline structures have provided a fundamental understanding of nanoscale details regarding point defect behavior at grain boundaries in polycrystalline materials[23–32] as well as interfaces in nanolayered metal composites.[33–35] Previous work has used atomistic simulations to examine the interaction of point defect and point defect clusters with grain boundaries in 2D columnar and 3D nanocrystalline metals. For example, Samaras and colleagues[24–27] have used molecular dynamics (MD) studies of nanocrystalline metals to show that grain boundaries act as sinks for self-interstitial atoms after nearby cascade events, which also leads to the formation of stacking fault tetrahedron in the grain interior for fcc Ni. Millett *et al.* used molecular dynamics simulations of 2D columnar nanocrystalline Mo to investigate the ability of grain boundaries to act as both a sink for point defects and a source for vacancies at high homologous temperatures ($T > 0.75T_m$).[28,29] While these studies are instrumental to understanding the operating mechanisms induced by radiation, these types of studies have numerous grain boundaries with many confounding effects. For instance, nanocrystalline microstructures contain complex grain boundaries with different tilt and twist misorientations, triple junctions, and a distribution of grain sizes. Hence it is often difficult to ascertain the influence of grain boundary character on the point defect-grain boundary interaction.

On the other hand, bicrystalline simulations can also be used to explore the influence of individual grain boundary structure on point defect behavior/properties using both *ab initio* and molecular dynamics simulations. *Ab initio* techniques have been used to explore properties for only a few low-Σ boundaries due to the high computational expense of accounting for the electronic structure. However, the relatively inexpensive cost of molecular dynamics simulations enables grain boundary studies that have yet to be realized using *ab initio* simulations because of the large number of atoms required or the time scales required. For example, displacement cascade (or collision cascade) simulations are one example of a computationally intensive simulation that requires both a large number of atoms and a long time scale for motion of defect species after the initial primary knock-on atom event. Pèrez-Pèrez and Smith used bicrystal MD simulations of a $\Sigma17(530)$ grain boundary to investigate the structural rearrangement and absorption of point defects following the cascade event.[31,32] They found that there are preferential sites within the boundary where defects tended to localize and that 85% of defects within the boundary are within a few Angstroms of the grain boundary center. More recently, Bai *et al.*[23] used MD simulations and temperature accelerated dynamics to show that grain boundaries can act as an effective sink for vacancies and interstitials through various mechanisms in Cu. In one such mechanism, interstitials are loaded into the boundary, which then acts as a source, emitting interstitials to annihilate vacancies in the bulk. Moreover, there are many studies that have explored point defect energetics in a few (predominantly low-Σ) grain boundaries. For example, Kwok, Ho, Yip, and colleagues[36–38] examined diffusion in an Fe $\Sigma5$ grain boundary by examining the mechanisms by which vacancies migrate at high temperatures. Also, Mishin and colleagues[39–41] investigated point defect properties of multiple low-Σ boundaries in Cu to understand grain boundary diffusion at low and high temperatures. Recently, Demkowicz *et al.*[42] investigated the effectiveness of $\Sigma3$ coherent twins to act as sinks for radiation-induced point defects in nanotwinned Cu. While these studies are instrumental to mechanisms and responses for several grain boundaries, it would also be beneficial to use the relatively low cost of bicrystal MD simulations to sample a larger distribution of boundaries and therefore understand how grain boundary character may impact the ability of grain boundaries to act as sinks for point defects. Moreover, this kind of study can provide a natural bridge to higher scale models by exploring extreme value statistics and uncertainty associated with grain boundary absorption of point defects and their associated binding energies.

Consequently, atomistic simulations that incorporate a large number of grain boundaries can shed light on how grain boundary character influences point defect-related properties in polycrystalline materials. While MD simulations are much less expensive than *ab initio* simulations, very few simulations consider a large number of grain boundaries in their analysis of grain boundary-related properties. However, it is well known that polycrystalline metals have a large range of grain boundary types and high-resolution transmission electron microscopy has shown large differences in grain boundary structures.[43–46] The exact nature of the atomic structure at the grain boundary plays an important role in material properties.[47,48] Hence, typically, MD simulations that consider a wide range of grain boundaries have focused on structure-energy relationships in fcc metals.[49–63] In their seminal work on grain boundary structure, Sutton and Vitek[49–51] investigated the structural elements that comprised symmetric and asymmetric tilt grain boundaries, how to classify these structural units, and their relationship to properties, such as the grain boundary energy. Wolf has investigated how grain boundary degrees of freedom (associated with the grain boundary structure) correlates with grain boundary (GB) energy for various grain boundary systems in fcc metals.[56–59] Holm *et al.* calculated energies of 388 GBs in Al, Au, Cu, and Ni and observed that the GB energy scales with the shear modulus.[60] Tschopp and McDowell have studied how the faceted atomic structure of asymmetric tilt grain boundary systems relates to grain boundary energy and structural units in Al and Cu.[63–65] How grain boundary character affects other properties has also been investigated. Olmsted, Foiles, and Holm calculated 388 distinct grain boundaries for Ni and Al and analyzed metrics for describing grain boundary energy as well as how grain boundary character influences grain boundary mobility.[66,67] McDowell, Spearot, Tschopp, Tucker, and colleagues[61,68–75] have investigated how grain boundary structure influenced grain boundary dislocation nucleation mechanisms. DeWald and Curtin[76–78] have shown assorted dislocation/grain boundary reactions for dislocation transmission through a range of grain boundary structures. Recently, Tschopp *et al.* used 50 symmetric tilt grain boundaries to show that interstitials have an energetic driving force to preferentially bind to grain boundary sites over vacancies.[79] With an emphasis for design of the next generation of radiation-tolerant materials, clearly a methodology that can analyze how point defect absorption is influenced by grain boundary character would be valuable.

Therefore, in this work, the research objective is to systematically investigate the influence of grain boundary character on the formation energetics and length scales of vacancies and self-interstitial atoms at grain boundaries at 0 K. Molecular statics are used to investigate the static energetics; the effect of entropy will need to be incorporated later to fully capture the absorption behavior of point defects at high temperatures. Iron is chosen as an ideal bcc structural material for this study. While our earlier work examined only ⟨100⟩ symmetric tilt grain boundaries,[79] herein symmetric tilt grain boundaries (STGBs) with ⟨100⟩, ⟨110⟩, and ⟨111⟩ tilt axes as well as twist and asymmetric tilt grain boundaries are chosen to investigate the vacancy and self-interstitial atom formation energies as a function of location within/around the grain boundary. In Sec. II, the methodology for generating a grain boundary structure database and for iteratively calculating vacancy and self-interstitial atom formation energies over all sites and all boundaries is presented. In Sec. III, we examine several aspects of this study: (1) the structures and energies of symmetric tilt grain boundaries used herein, (2) the relative influence of grain boundary atomic structure on point defect formation energies, (3) the influence of macroscopic grain boundary character on defect formation energies, and (4) the grain boundary site preference, site density, and site strength. The scope of this research is to investigate these trends for pristine, minimum energy grain boundaries; higher energy grain boundary structures were not examined herein. The simulation results show not only how local atomic structure and grain boundary character affect the formation energetics of point defects, but also provide grain boundary site metrics and necessary length scale parameters for potential inclusion in higher scale models.

II. SIMULATION METHODOLOGY

The methodology used to calculate the point defect energetics at the grain boundary is similar to approaches used in previous studies (e.g., Refs. 39 and 41). Figure 1 shows a schematic of the process used to examine the influence of grain boundary character on vacancy and self-interstitial atom (SIA) absorption to grain boundaries. The methodology used here is grouped into three primary steps: initialize, test, and analyze. First, in the initialization step, the grain boundary structure database is generated. Then, during the test step, grain boundaries are selected from this database and defects are iteratively added to grain boundary sites to calculate their formation energies. Last, during the analyze step, the calculated database of properties is examined to determine the influence of important factors, such as local atomic structure, distance from the grain boundary, and grain boundary character (misorientation angle, Sigma value, etc.).

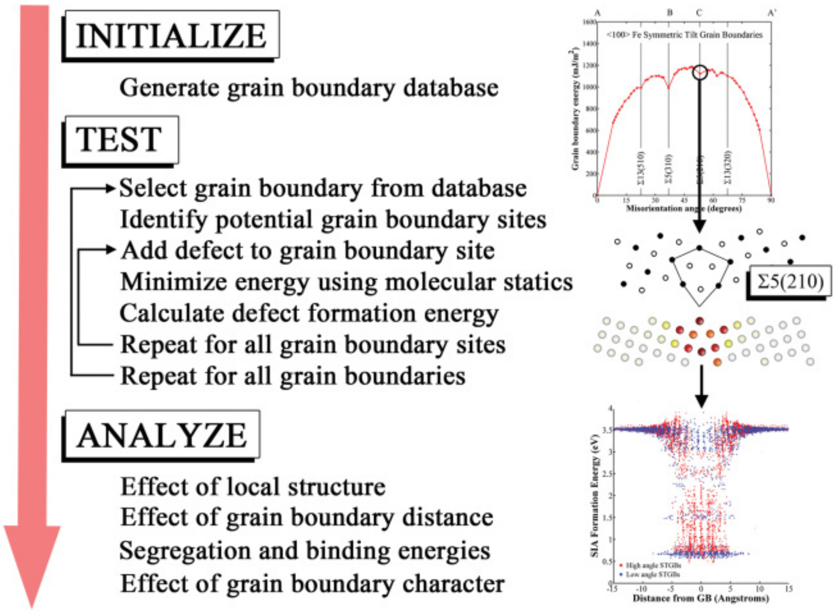

FIG. 1. (Color online) Schematic of the process used to initialize, test, and analyze point defects in grain boundaries. The example to the right shows a grain boundary system from which a single grain boundary is selected and then the point defect formation energy of every potential grain boundary site is subsequently tested to build a database of formation energies.

The grain boundary structure database was generated using a parallel molecular dynamics code, LAMMPS.[80] The equilibrium 0 K structure and energy for each grain boundary was calculated using a bicrystal computational cell with 3D periodic boundary conditions consisting of two grains.[81] The minimum distance between the two periodic boundaries in each computational cell was 12 nm. As with previous work, multiple initial configurations with different in-plane rigid body translations and an atom deletion criterion were used to access the minimum energy GB structures (e.g., Refs. 63, 64 and 66). The Polak-Ribière nonlinear conjugate gradient algorithm was used for the energy minimization process, whereby the simulation cell was also allowed to expand normal to the grain boundary plane.[56] Hundreds to thousands of potential atomic structures were sampled to generate each minimum energy structure. Hence, Vitek and colleagues have shown that each grain boundary can be composed of a multiplicity of different atomic structures at the grain boundary,[52–55] which are related to the arrangement of grain boundary dislocations and can ultimately result in different grain boundary properties. In contrast to the aforementioned work, the concentration here was on the minimum energy boundary structure of a large number of boundaries as opposed to a range of atomic structures for a few boundaries. Therefore a grain boundary structure database with ≈170 minimum energy grain boundaries was generated to assess the influence of grain boundary character on the binding energy of vacancies and interstitials. This database primarily contains ⟨100⟩, ⟨110⟩, and ⟨111⟩ symmetric tilt grain boundaries along with some asymmetric tilt grain boundaries and symmetric twist grain boundaries. For initial generation of the structures, the updated Mendelev *et al.*[82] interatomic potential was used.[83] The Mendelev *et al.* Fe potential is based on the embedded atom method formulation[84,85] and performs very well with respect to DFT values pertinent to radiation damage studies.[86]

After generating the grain boundary database, the next step is to examine the formation energies of vacancies and self-interstitial atoms for various grain boundaries. As an initial example, consider the $\Sigma5(210)\theta = 53.13^\circ$ symmetric tilt grain boundary shown in Fig. 1. First, the $\Sigma5(210)\theta = 53.13^\circ$ grain boundary structure is obtained from the grain boundary structure database and all grain boundary sites within 15 Å are identified (47 sites). Then, one grain boundary site is selected and a point defect is added by either removing the atom at that site (vacancy) or adding an additional atom at a nearby interstitial position (self-interstitial atom). For the interstitial atoms, the atom was added approximately 0.5 Å along the grain boundary period direction (perpendicular to the tilt direction in the grain boundary plane). Next, the simulation cell is relaxed through a nonlinear conjugate gradient energy minimization process and the total energy with the point defect is obtained. For vacancies, the formation energy for a particular site α, E^{α}_{vf}, is calculated by

$$E^{\alpha}_{\mathrm{vf}} = E^{\alpha}_{\mathrm{GB,v}} - E_{\mathrm{GB}} + E_{\mathrm{coh}}. \qquad (1)$$

Here, E_{coh} is the cohesive energy/atom of a perfect bcc lattice, and $E^{\alpha}_{\mathrm{GB,v}}$ and E_{GB} are the total energies of the simulation cell with and without the vacancy. On the other hand, for self-interstitial atoms, the formation energy for a particular site α, $E^{\alpha}_{\mathrm{SIA},f}$, is calculated by

$$E^{\alpha}_{\mathrm{SIA},f} = E^{\alpha}_{\mathrm{GB,SIA}} - E_{\mathrm{GB}} - E_{\mathrm{coh}}, \qquad (2)$$

where $E^{\alpha}_{\mathrm{GB,SIA}}$ is the total energy of the simulation cell with the self-interstitial atom placed at site α. Once these two simulations have run and the formation energies have been calculated, then this procedure is repeated for the other grain boundary sites [e.g., the other 46 sites for the $\Sigma5(210)\theta = 53.13^\circ$ grain boundary]. After the formation energies for all grain boundary sites have been calculated, then another grain boundary structure is obtained from the grain boundary structure database and the process is repeated until all grain boundaries have been sampled. This process provides a grain boundary property database of formation energies of point defects over numerous grain boundary structures.

The strength of each grain boundary as a sink for point defects is of particular interest in the present study. In an attempt to quantify the grain boundary sink strength, we examine several potential metrics for the distribution of point defect formation energies at each boundary. The first metric to be examined is the minimum formation energy or the extreme value of this distribution, which may be indicative of the strength of the boundary to absorb point defects. However, it should also be mentioned that this quantity will likely change as point defects are absorbed into the boundary, thereby locally altering the grain boundary structure. So, while this extreme value of the formation energy distribution may be important as to the *potential* change in energy due to absorption of a point defect by a particular boundary site, the *mean* change in energy may also shed light onto the overall strength of each boundary. Therefore the second metric to be examined is the mean point defect formation energy, which will be comparatively insensitive to absorption of multiple point defects, but will not capture the extreme values of the formation energy distribution. The two metrics will help facilitate comparisons in the "sink strength" of boundaries between different grain boundary degrees of freedom and types (e.g., tilt versus twist, symmetric versus asymmetric, etc.).

In the first part of the present work, we chose to focus mainly on the ⟨100⟩, ⟨110⟩, and ⟨111⟩ symmetric tilt grain boundary systems. In general, grain boundaries in these systems are easier to obtain a global minimum energy structure than for asymmetric boundaries.[61,66,87] While substantial care was taken to sample a wide range of configurations for each boundary, in some instances negative point defect formation energies indicate that a lower grain boundary energy can be obtained through adding/removing an atom from the grain boundary; subsequently, these boundaries were removed from analyses that considered the minimum formation energies. There are a total of 135 grain boundaries that contained all positive formation energies (50 ⟨100⟩, 38 ⟨110⟩, and 25 ⟨111⟩ symmetric tilt boundaries, 15 twist boundaries, and seven asymmetric tilt boundaries). In a later analysis of mean grain boundary properties, additional boundaries are included to help illustrate trends (171 total). The subsequent analysis of this grain boundary property database with respect to local atomic structure, distance from the grain boundary and grain boundary metrics is presented in Sec. III.

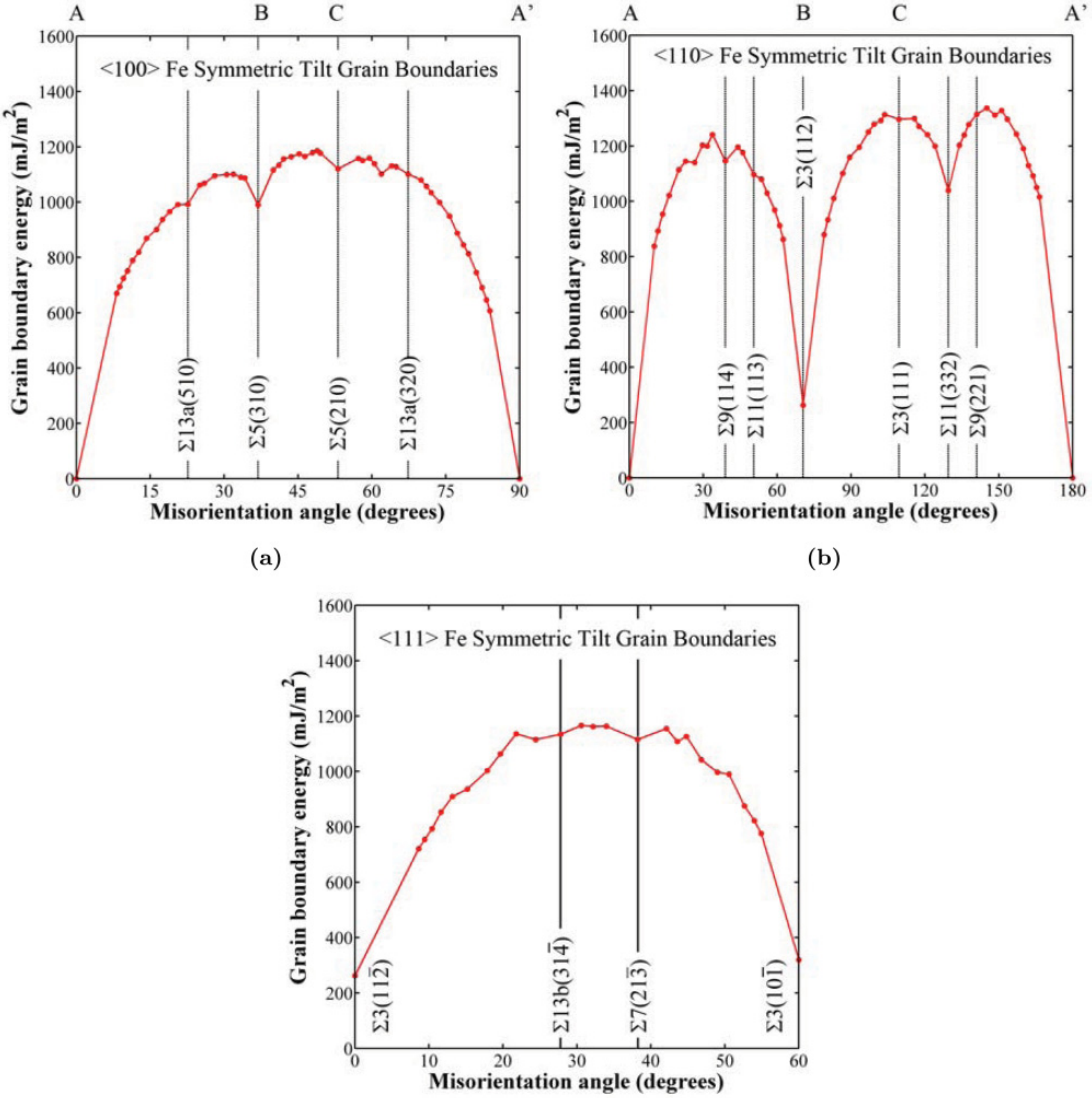

(a)

(b)

(c)

FIG. 2. (Color online) Symmetric tilt grain boundary misorientation-energy relationship for (a) the ⟨100⟩ tilt axis, (b) the ⟨110⟩ tilt axis, and (c) the ⟨111⟩ tilt axis. The low Σ grain boundaries (Σ ⩽ 13) in each system are identified. The strongest cusps are the Σ3(112), the Σ11(332), and the Σ5(310) boundaries.

III. SIMULATION RESULTS

A. Examining the structures and energies of symmetric tilt grain boundaries

The structures and energies of symmetric tilt grain boundaries may be important for understanding the interaction between radiation-induced point defects and the boundary. Figures 2(a)–2(c) show the grain boundary energy as a function of misorientation angle for the ⟨100⟩, ⟨110⟩, and ⟨111⟩ symmetric tilt grain boundaries, respectively. The low order coincident site lattice (CSL) systems (low Σ value, Σ ⩽ 13) are also shown for each of the STGB systems: the Σ5 and Σ13a GBs for the ⟨100⟩ STGBs, the Σ3, Σ9, and Σ11 GBs for the ⟨110⟩ STGBs, and the Σ3, Σ7, and Σ13b GBs for the ⟨111⟩ STGBs. For the ⟨100⟩ tilt axis, only minor cusps are observed in the energy relationship, most noticeably at the Σ5(310) STGB (990 mJ/m^2) in the ⟨100⟩ tilt system. However, for the ⟨110⟩ tilt axis, the grain boundary energy varies strongly with misorientation angle. The two deep cusps are the Σ3(112) twin boundary (262 mJ/m^2) and the Σ11(332) STGB (1039 mJ/m^2). The ⟨111⟩ tilt system also displays a cusp at the Σ3(112) twin boundary. In addition to many

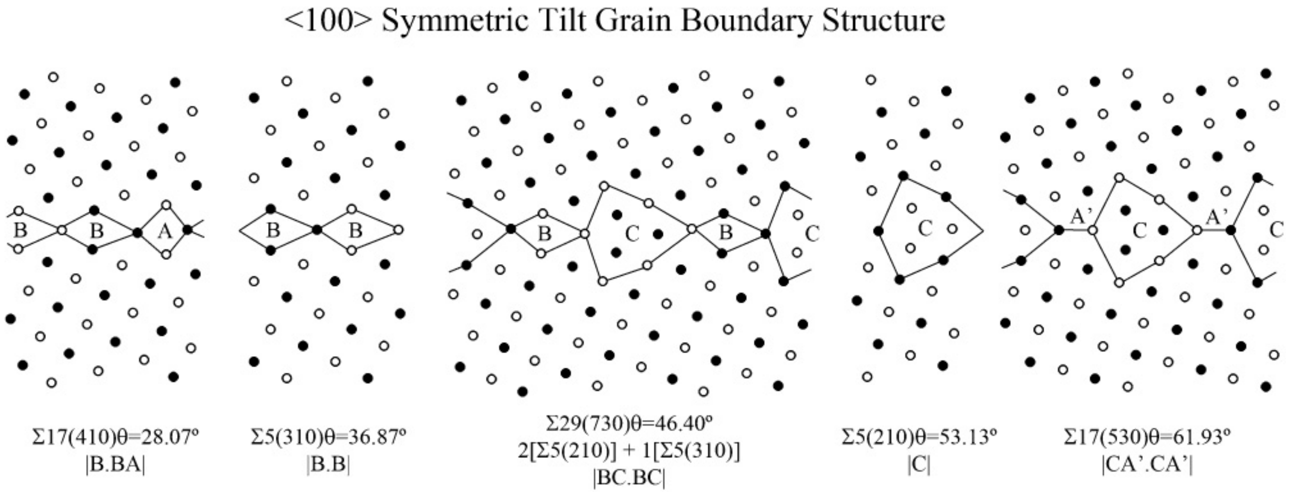

Σ17(410)θ=28.07°
|B.BA|

Σ5(310)θ=36.87°
|B.B|

Σ29(730)θ=46.40°
2[Σ5(210)] + 1[Σ5(310)]
|BC.BC|

Σ5(210)θ=53.13°
|C|

Σ17(530)θ=61.93°
|CA'.CA'|

FIG. 3. ⟨100⟩ symmetric tilt grain boundary structures with structural units outlined for the Σ17(410), Σ5(210), Σ29(730), Σ5(310), and Σ17(530) boundaries. Black and white denote atoms on different {100} planes. The different structural units are labeled A, B, C, and A'. The Σ29(730) is composed of structural units from the two favored Σ5 boundaries in a ratio determined by the structural unit model.[51,90,91]

high-angle boundaries, several low-angle boundaries ($\leqslant 15^\circ$) were also generated.

The grain boundary structure and energy have a very defined relationship. For low-angle boundaries, the grain boundary is composed of an array of discrete dislocations and the corresponding energy can be calculated based on the classic dislocation model of Read and Shockley.[88] For high-angle boundaries, the spacing between lattice dislocations is small enough that dislocation cores overlap and the rearrangement of dislocation cores forms a local atomic structure within the grain boundary.[89] Sutton and Vitek analyzed the grain boundary structure by characterizing the local atomic structure as structural units[49–51] and then the atomic structure of tilt grain boundaries can be predicted using the structural unit model.[51,90,91] The structural unit model works as follows. Grain boundaries with certain misorientation angles (and typically a low Σ value) can correspond to "favored" structural units, while all other boundaries are characterized by structural units from the two neighboring favored boundaries. In general, this relationship holds for many pure tilt and twist boundary types with low index rotation axes. However, the structural unit model may not adequately describe the atomic structure in boundaries where dislocations readily dissociate[81,87] or for mixed tilt-twist boundaries.[92] Figure 3 shows an example for the ⟨100⟩ STGB system, where the two Σ5 boundaries are favored STGBs and the Σ29(730) boundary is a combination of structural units from the two Σ5 boundaries. The structural units for the Σ5{310} and Σ5{210} STGBs are labeled B and C, respectively. Also, notice that the ratio of structural units in the Σ29 GB can be determined by the crystallographic relationship of the two favored boundaries, i.e., Σ29(730) = 2[Σ5(210)] + 1[Σ5(310)]. In a similar manner, the two Σ17 boundaries are combinations of the favored B and C structural units and "structural units" of the perfect lattice, A and A'.

A similar relationship for grain boundary structural units exists for the ⟨110⟩ symmetric tilt grain boundary system as well. Figure 4 shows the structural units for several low-order CSL grain boundaries in the ⟨110⟩ symmetric tilt grain boundary system (Σ3, Σ9, Σ11, Σ17, Σ19, Σ27, Σ33). For this system, the two Σ3 grain boundaries are favored boundaries with the B and C structural units, respectively. Also, the $\theta = 0^\circ$ and 180° single crystal favored grain boundaries contain the A and A' structural units (perfect lattice). Grain boundaries at intermediate misorientation angles are composed of structural units of the adjacent favored boundaries. This example shows the structural units of the ⟨110⟩ tilt system, but each class of grain boundaries (e.g., ⟨100⟩ tilt, ⟨110⟩ tilt, ⟨111⟩ tilt) in this paper has its own favored boundaries and structural units. Additionally, the ratio and location of different structural units leads to different internal elastic strain fields within each boundary; therefore the properties of grain boundaries with intermediate misorientation angles is not easily determined through a linear relationship between the favored boundaries, as can be observed from the grain boundary energy plots in Fig. 2.

B. Analyzing the influence of grain boundary atomic structure on point defect formation energies

In this section, the vacancy and interstitial formation energies are examined as a function of the local atomic structure and distance from the center of the grain boundary. For the sake of brevity, the ⟨100⟩ symmetric tilt grain boundary system is presented herein. Formation energies from other grain boundary systems will be added in subsequent sections.

Examining how local atomic structure and grain boundary sites contribute to the formation energy of point defects is important for understanding defect absorption behavior. Figure 5 shows the vacancy and interstitial formation energies that correspond to atomic positions in three ⟨100⟩ symmetric tilt grain boundary structures shown in Fig. 3. In this plot, the relaxed point defect formation energies are shown in the unrelaxed atomic sites; realize that there is a 0.5 Å shift between the unrelaxed atomic sites for the interstitial atoms and vacancies, but we have shifted the unrelaxed interstitial atom sites by 0.5 Å to coincide with the vacancy sites due to the grain boundary periodicity. Note that in subsequent

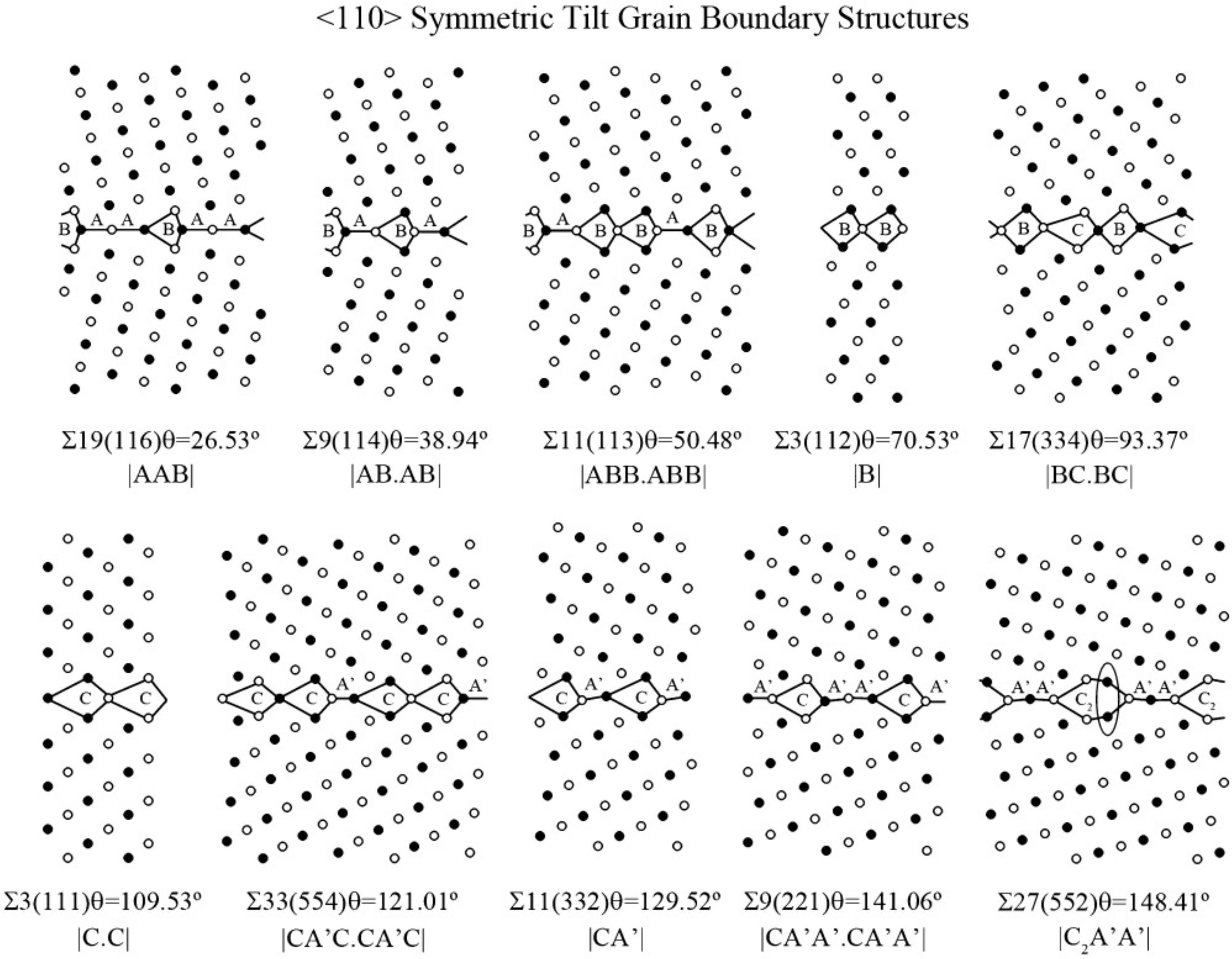

FIG. 4. ⟨110⟩ symmetric tilt grain boundary structures with structural units outlined for numerous boundaries, including the "favored" Σ3(112) and Σ3(111) boundaries. Black and white denote atoms on different {110} planes. The different structural units are labeled as in Fig. 3. Similar to Fig. 3, the structural units of intermediate misorientations can be determined from the structural units of the favored boundaries.

plots, we have used the unrelaxed atomic sites due to the difficulty of defining the relaxed vacancy location and to facilitate direct comparison between interstitial atoms and vacancies. The color bar in the upper (lower) set of images corresponds to grain boundary sites with formation energies lower (higher) than in the bulk. The vacancy and SIA color bar is normalized by the corresponding formation energy in the bulk. In general, grain boundary sites associated with atoms in the "B" and "C" structural units and nearby these structural units tend to have lower formation energies than in the bulk lattice (for both vacancies and SIAs). Moreover, since the color represents the fraction of the bulk formation energy, these contours show that the formation energies for interstitial atoms at the boundary have a much lower formation energy (relative to the bulk formation energy) than vacancies. So, while there is a similar formation energy for vacancies and interstitials (in agreement with previous simulations, e.g., Refs. 39, 40 and 41), the fraction of the bulk formation energies is much lower for interstitials, which leads to higher binding energies to grain boundaries. Subsequently, there is a corresponding larger energetic driving force for interstitials to segregate to the boundary in Fe over vacancies.[79]

Grain boundary sites with a higher formation energy may also be important for understanding interfacial absorption of point defects. In Fig. 5, there are atoms lying at the intersection of structural units along the grain boundary plane that have a higher vacancy formation energy than the bulk, i.e., it is energetically more favorable for the vacancy to occupy a bulk lattice site. Interestingly, the corresponding sites for interstitial atoms do not have a higher formation energy, but rather a much lower formation energy. However, both vacancies and interstitials have some sites outside of the outlined structural units that also have higher formation energies than in the bulk lattice. These sites may be significant for defect absorption if they present an energy barrier for diffusion to the boundary or within the grain boundary. However, in these cases and for the cases shown later, the magnitude of the formation energy increase is much smaller when compared to the magnitude of the potential formation energy decrease at numerous grain boundary sites.

Low-angle grain boundaries also interact with point defects in the lattice. Figure 6 shows the vacancy and interstitial formation energies for two low-angle grain boundary structures ($\theta \leqslant 15^\circ$) in the ⟨100⟩ tilt system. The two boundaries

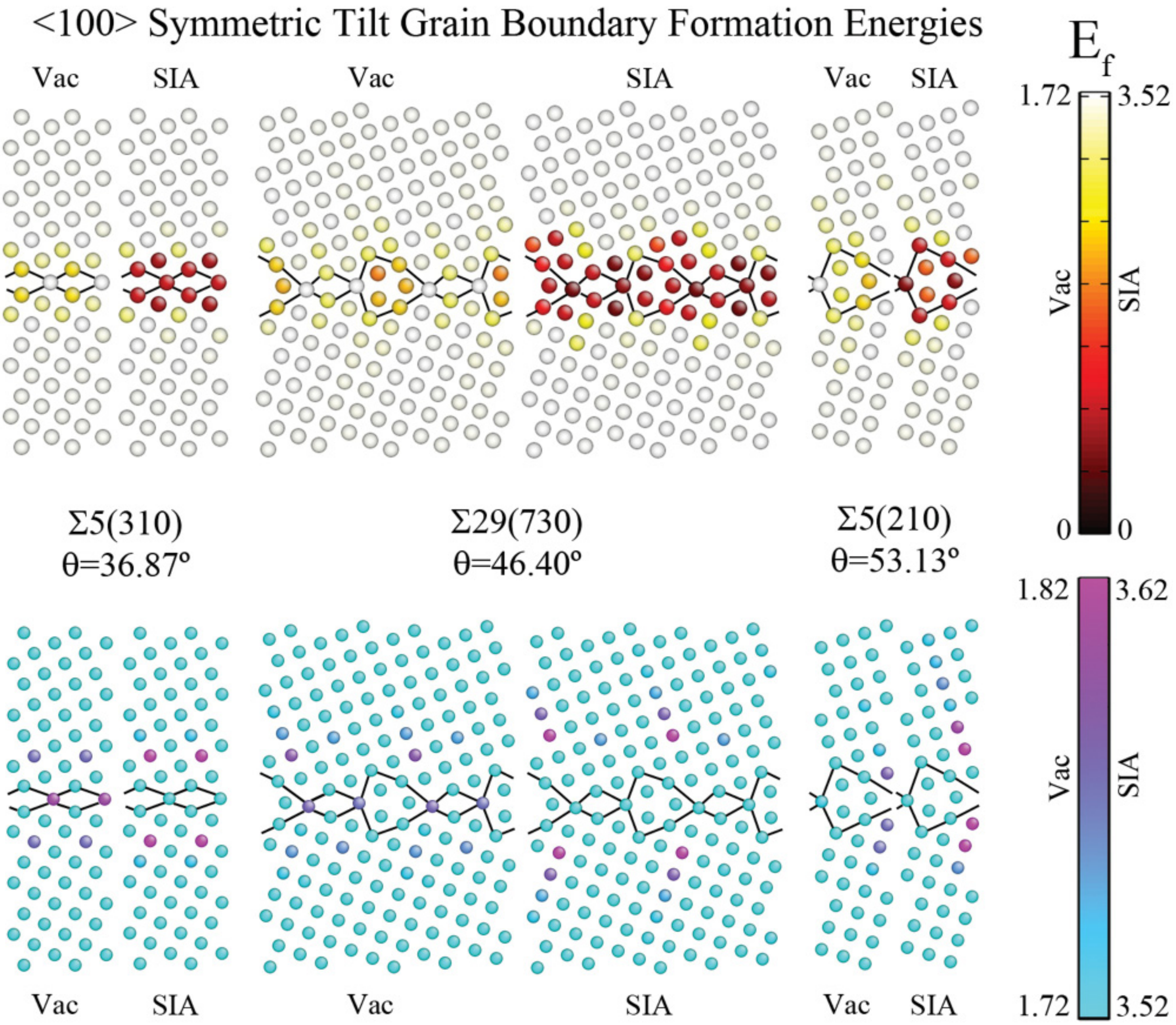

FIG. 5. (Color online) Vacancy and interstitial formation energies as a function of spatial position for three ⟨100⟩ symmetric tilt grain boundaries: Σ5(210), Σ29(730), and Σ5(310) boundaries. The upper (lower) images show the distribution of formation energies lower (higher) than bulk values. The point defect formation energies are shown in the unrelaxed position; while the interstitial atoms are placed 0.5 Å away from the vacancy sites, the atoms are shown in the same location due to the grain boundary periodicity. The structural units are outlined and correspond to those shown in Fig. 3.

are the $\Sigma41(910)\theta = 12.68^\circ$ low-angle boundary and the $\Sigma85(760)\theta = 81.20^\circ$ low-angle boundary ($\theta_{\text{eff}} = 8.80^\circ$ when lattice symmetry is accounted for). The discrete dislocations that make up the grain boundary structure are shown. Multiple low formation energy sites for both vacancies and interstitials surround the discrete dislocations that make up the low misorientation angle between the two grains. Again, compared to vacancies, the self-interstitial atoms have much lower formation energies relative to formation energies in the bulk lattice. Interestingly, the dislocation type necessary for the $\Sigma41(910)\theta = 12.68^\circ$ and $\Sigma85(760)\theta = 81.20^\circ$ low-angle boundaries impacts both the size and shape of the region with lower local formation energies for point defects. For instance, in the case of the $\Sigma85(760)\theta = 81.20^\circ$ low-angle boundary, even atoms that are close to 8 Å away still have a low vacancy formation energy. However, as the misorientation angle increases, the spacing between dislocations decreases and the affected regions begin to merge as the dislocation cores start to overlap. On the other hand, as the misorientation angle decreases, the low-angle boundaries behave the same as isolated dislocations in a perfect lattice. Hence, low-energy low-angle boundaries will tend to have similar defect interaction properties as single dislocations within the lattice. Last, the lattice between the dislocations has formation energies comparable to the perfect single crystal, as would be expected.

The vacancy and interstitial formation energies for each grain boundary site as a function of position can provide insight into the length scale associated with point defect absorption by each boundary. Figures 7(a) and 7(b) plot the vacancy and interstitial formation energies, respectively, as a function from distance from the grain boundary for all 50 ⟨100⟩ symmetric tilt grain boundaries. For this plot, all grain boundaries were first centered such that the formation energies are symmetric about a value of 0 Å for the grain boundary distance. Then,

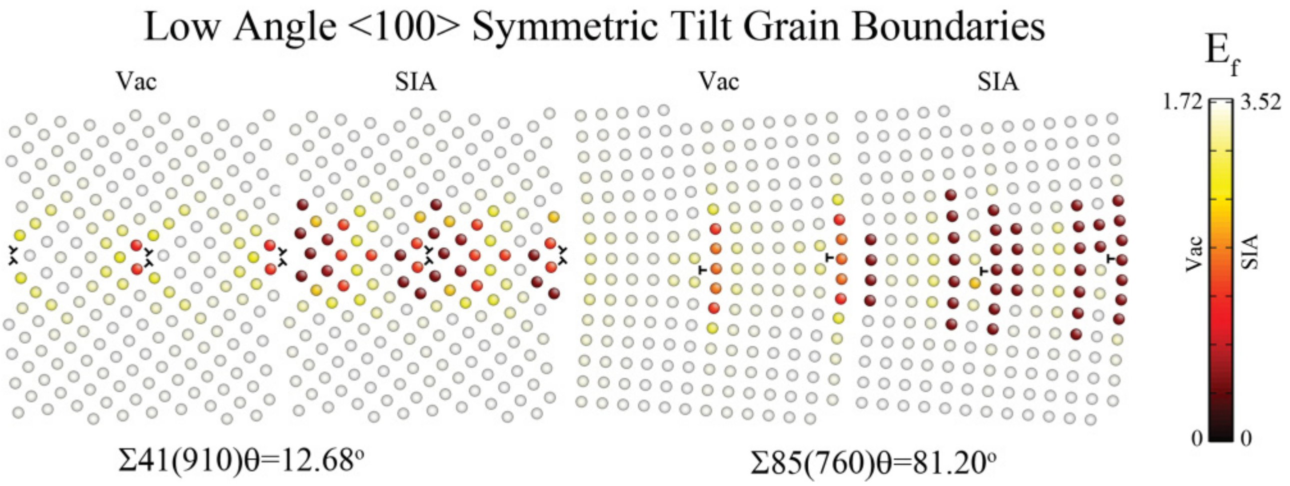

FIG. 6. (Color online) Vacancy and interstitial formation energies for two low-angle boundaries in the ⟨100⟩ symmetric tilt grain boundary system: the $\Sigma41(910)\theta = 12.68^\circ$ and $\Sigma85(760)\theta = 81.20^\circ$ grain boundaries. As in Fig. 5, the point defect formation energies are shown in the unrelaxed position with formation energies for interstitial atoms and vacancies shown in the same location due to periodicity. The affected region of lower defect formation energies surrounding the dislocations is noticeably larger for interstitials than for vacancies.

a misorientation angle of 15° was used as a threshold for classifying boundaries as either low- or high-angle grain boundaries. First, for vacancy formation energies in Fig. 7(a), the majority of vacancy formation energies in the boundary have values that are much lower than the bulk values as well as a few energies that are slightly higher than bulk values. Second, the vacancy formation energies approach bulk values between 5–8 Å away from the center of the grain boundary. Third, for vacancy formation energies, the low-angle boundaries tend to behave very similarly to high-angle boundaries, aside from a few boundaries that show a band of lower formation energies associated with dislocations along the {110} plane (inset image). Last, for vacancy formation energies, the data shows a symmetric relationship with both the minimum *and* maximum formation energies at a distance of ≈0 Å. So, while it is energetically favorable for vacancies to reside along the grain boundary plane, possibly due to coincidence between the adjoining lattices, there are also energetically unfavorable sites along this plane as well (as shown in Fig. 5).

For interstitial formation energies in the ⟨100⟩ tilt system [see Fig. 7(b)], there are some similarities with vacancies, but also some notable differences. First, there is a definitive contrast between low- and high-angle boundaries for interstitial formation energies. In the grain boundary region (≈5–8 Å from center), the low-angle boundaries tend to have either very low formation energies (discrete dislocation regions) or values comparable to bulk formation energies (intermediate single crystal regions). On the other hand, for high-angle boundaries, the majority of interstitial formation energies are much lower than in the bulk lattice with very few points that are comparable to bulk lattice formation energies. Second, in the low-angle boundaries, notice a much larger and more prominent clustering of low interstitial formation energies than those obtained for vacancy formation energies. Moreover, there is a much wider absorption length scale for interstitials in low-angle grain boundaries. Last, as opposed to Fig. 7(a), the minimum formation energies are distributed throughout the grain boundary (within ±5 Å of the grain boundary center).

The ability to describe grain boundaries in terms of dislocations may lead to an improved understanding of point defect interactions with grain boundaries. There have been a number of studies that have focused on the dislocation structure of heterogeneous interfaces on point defect interactions. For example, in Cu-Nb multilayered composites, the detailed interactions between vacancies, interstitials, and the interfacial misfit dislocations may help explain the ability for this material system to mitigate radiation-induced point defects.[34,93–95] With respect to coherent interfaces (grain boundaries), low-angle grain boundaries have similar defect interaction properties to discrete lattice dislocations. There have been a number of studies that investigate the interaction between lattice dislocations and vacancies by means of atomistic simulations. For instance, several decades ago, Ingle and Crocker[96] used simple pair potentials to investigate the interaction between vacancies and edge dislocations in bcc iron and show that the maximum vacancy-dislocation binding energy is ≈50% of the vacancy formation energy. As can be seen from Fig. 7(a), the present study shows that there is a band of vacancy formation energies for low-angle boundaries in the ⟨100⟩ tilt system that have binding energies of ≈60% of the bulk vacancy formation energy, in agreement with Ingle and Crocker's study.[96] More recent work has used atomistic simulations of vacancy-dislocation interactions to compare with elasticity and show that linear elastic predictions agree when the cores of the two defects do not overlap.[97] Other studies have examined vacancy-dislocation interactions in dislocation climb processes in iron.[98] Additionally, there have been multiple studies that have investigated the energetics of interaction of vacancies, interstitials, and He with dislocations.[99–104] Interestingly, these studies of lattice dislocation and defect interactions can also be interpretted in terms of low-angle grain boundary behavior as well. As dislocation cores begin to overlap, though, the stress fields and energies of high-angle grain boundaries may best be represented through disclination defects rather than dislocation models (e.g., disclination structural unit model[105–108]).

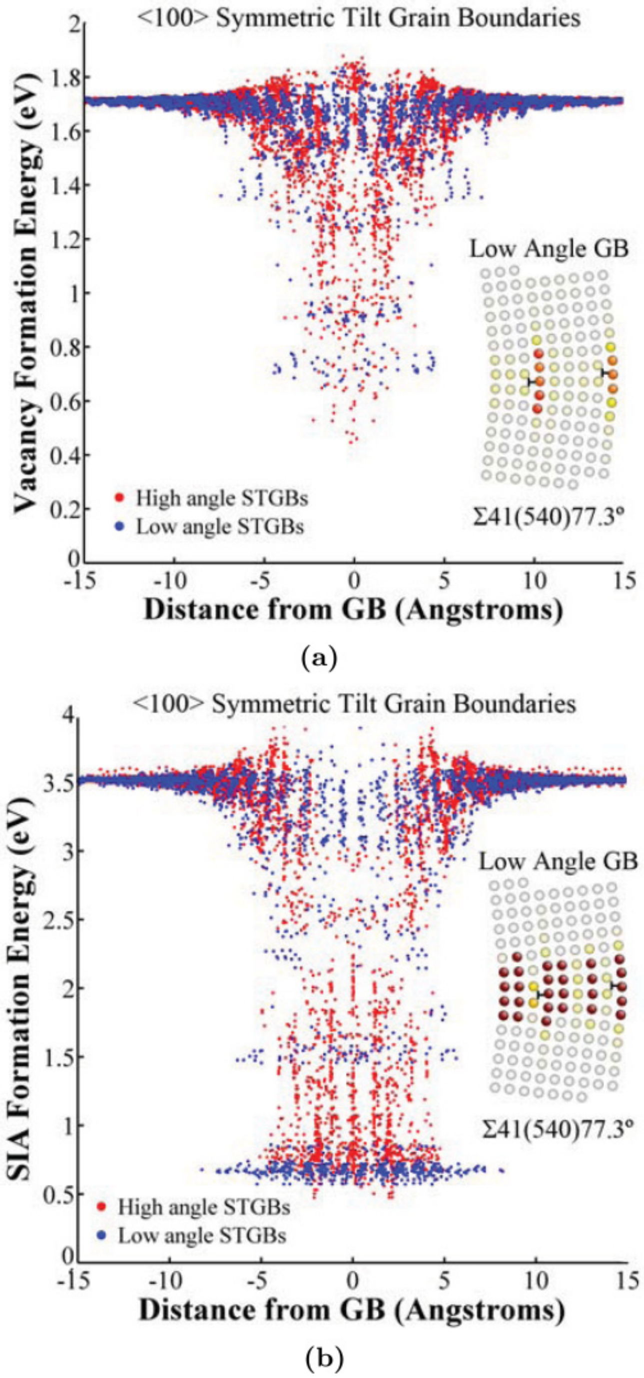

FIG. 7. (Color online) (a) Vacancy and (b) interstitial formation energies as a function of distance from the grain boundary for all $\langle 100\rangle$ symmetric tilt grain boundaries. The vacancy and interstitial distances are the unrelaxed distances to facilitate comparison. The point defect formation energies are lower in the grain boundary region, which extends ≈5 Å from the center of the boundary for the $\langle 100\rangle$ tilt system.

C. Investigating the influence of macroscopic grain boundary character on defect formation energies

The macroscopic grain boundary character can also play a role in the absorption of point defects to the grain boundary. To explore the influence of grain boundary character on point defect absorption, we plotted (i) the distribution of defect formation energies (vacancies and interstitial atoms) and (ii) the mean defect formation energies against several grain boundary metrics: disorientation angle, grain boundary energy, and the Σ value of the boundary. Here, the term disorientation angle is defined as the minimum misorientation angle when accounting for lattice symmetry. The Σ value represents the inverse fraction of coincident sites if the two adjoining lattices are viewed as interpenetrating and, in some cases, have been associated with properties that are different from general high-angle grain boundaries.

Figures 8(a) and 8(c) show the vacancy and interstitial formation energy distributions as a function of the disorientation angle for $\langle 100\rangle$, $\langle 110\rangle$, and $\langle 111\rangle$ symmetric tilt grain boundaries. The minimum formation energy for each boundary is plotted as a separate symbol. Additionally, the single-crystal bulk formation energy value is drawn as a solid line. First, the minimum vacancy and interstitial formation energy appears to slightly decrease with increasing disorientation angle. However, this trend is largely influenced by the different classes of symmetric tilt grain boundaries. Notice that most grain boundaries within the same tilt system ($\langle 100\rangle$, $\langle 110\rangle$, or $\langle 111\rangle$) have very similar formation energies aside from a few "special" boundaries (the $\Sigma 5\{310\}$ and $\Sigma 5\{210\}$ STGBs, and the $\Sigma 3\{112\}$ STGB) that have minimum formation energies higher than the rest. Second, notice that the special boundaries have a larger influence on the vacancy formation energy than the interstitial formation energy, which is still much lower than that in the bulk (red line). It is also interesting to note that many of these low-Σ boundaries are often used in *ab initio* calculations because of their small periodic distances, but that these same boundaries may have properties that are in fact very different from general low- and high-angle boundaries. Last, the $\langle 100\rangle$ and $\langle 111\rangle$ tilt systems have comparable formation energies, while the $\langle 110\rangle$ tilt grain boundary system has much lower minimum formation energies. One possible explanation of this behavior is the difference in the interplanar spacing in the tilt direction between these different tilt systems, where the $\langle 110\rangle$ system has a much larger interplanar spacing compared to the $\langle 100\rangle$ and $\langle 111\rangle$ systems ($0.707a$ versus $0.500a$ and $0.288a$, respectively). Interestingly, low formation energies for both defect types correlate with this interplanar spacing, though.

Another way to analyze the formation energy distributions within these grain boundaries is to examine the effect of disorientation angle on the mean point defect formation energies, as shown in Figs. 8(b) and 8(d) for vacancies and self-interstitial defects. (The mean point defect formation energy used herein includes all atoms within 15 Å of the boundary center; while this results in a number of atoms with bulk formation energies being included in the calculation, this metric is unbiased with respect to the differences between different boundary types.) In these plots, additional symmetric/asymmetric tilt and twist grain boundaries are added to span a wider range of boundaries. For high-angle boundaries ($\theta > 15°$), there is very little correlation with disorientation angle for both vacancies and interstitials. Many of the added twist and asymmetric boundaries have low mean formation energies that do not monotonically correlate with disorientation angle. However, for low-angle boundaries ($\theta < 15°$), there is a much stronger correlation with disorientation angle; as disorientation

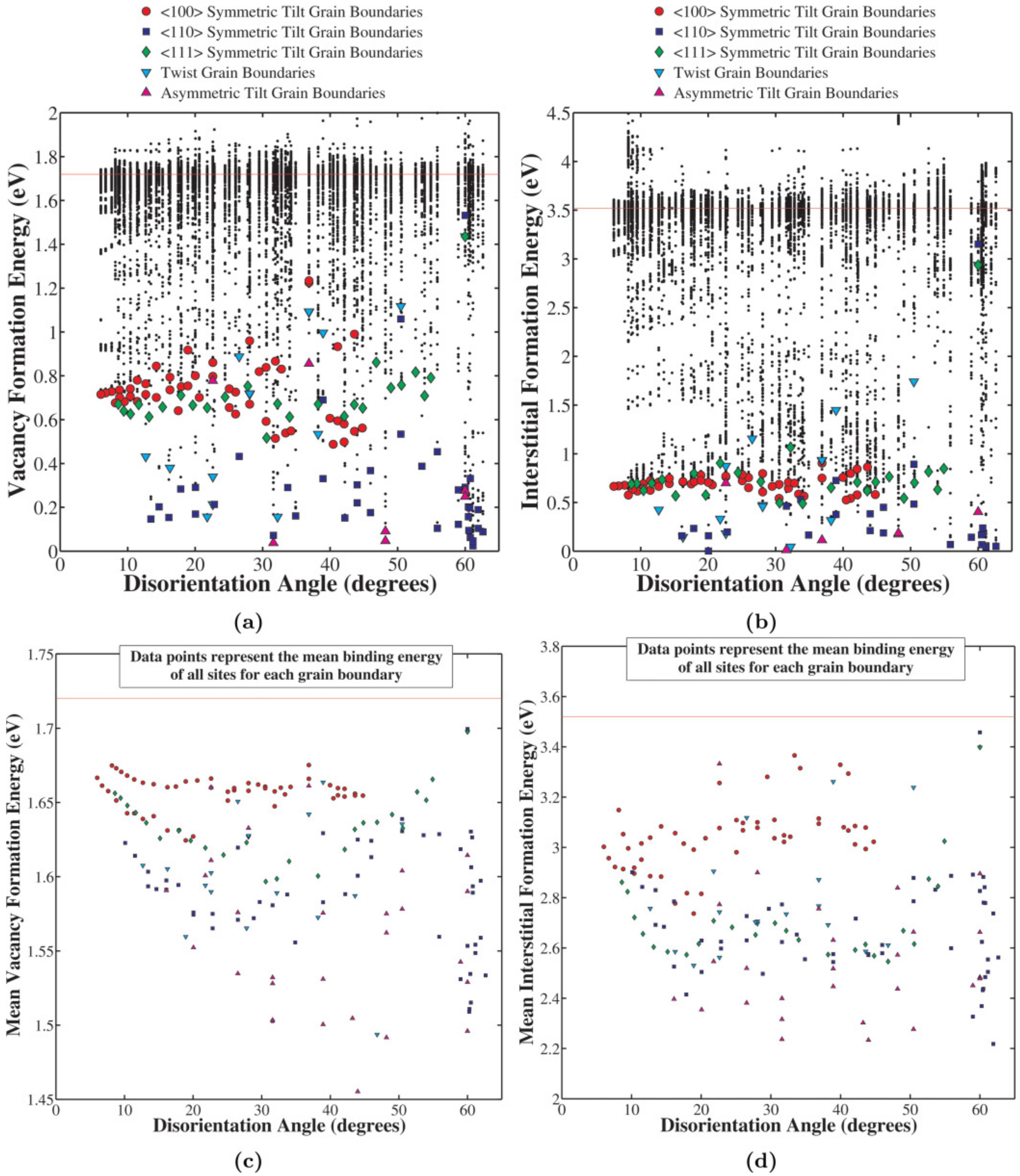

FIG. 8. (Color online) Vacancy (a) and (b) and interstitial (c) and (d) formation energies as a function of the disorientation angle for ⟨100⟩, ⟨110⟩, and ⟨111⟩ symmetric tilt grain boundaries. (a) and (c) The distribution of formation energies is plotted (black dots) as well as the minimum formation energy for each grain boundary (symbol). (b) and (d) The mean formation energy for each grain boundary is plotted against disorientation angle; additional twist and asymmetric grain boundaries are added to show the trend.

angle increases, the vacancy and interstitial formation energies decrease. This trend is especially strong for the case of vacancy formation energies. For ⟨100⟩ boundaries, there are two distinct clusters of data points, which correspond to the different dislocation types forming the low-angle boundary, as shown in Fig. 6 (the cluster with lower formation energies

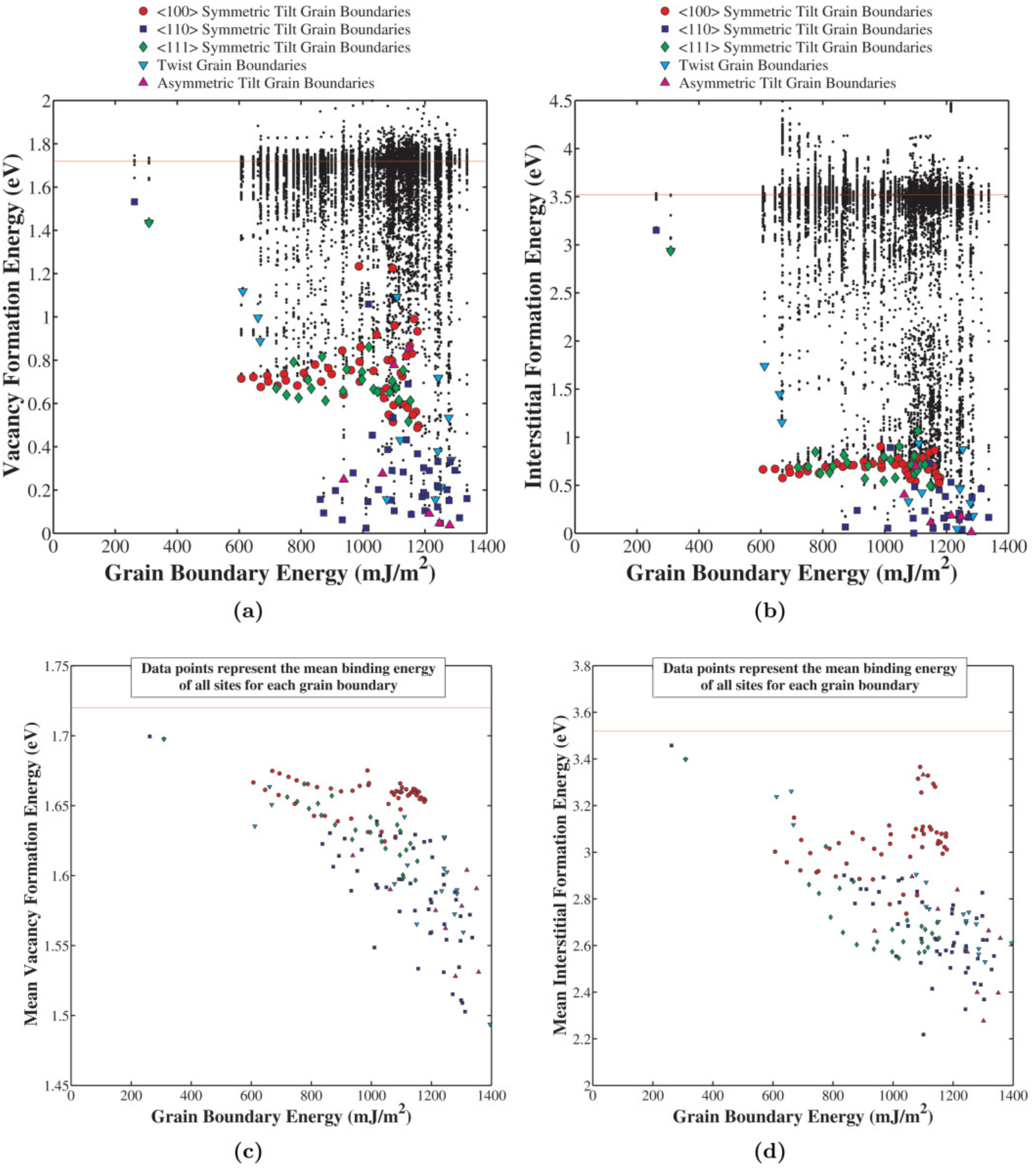

(a) (b)

(c) (d)

FIG. 9. (Color online) Vacancy (a) and (b) and interstitial (c) and (d) formation energies as a function of the grain boundary energy for ⟨100⟩, ⟨110⟩, and ⟨111⟩ symmetric tilt grain boundaries. The symbols denote the minimum (a) and (c) and mean formation energy (b) and (d) for each grain boundary, as in Fig. 8. The strongest trend occurs between the grain boundary energy and the mean defect formation energies (c) and (d).

corresponds to low-angle boundaries similar to the Σ85 STGB). In this case, the different dislocation types have both different length scales associated with trapping point defects and different formation energy distributions, which equates into slightly different mean responses that follow a similar trend. Trend lines are shown merely as a guide to the eye.

Figure 9 shows the vacancy and interstitial formation energy distributions as a function of the grain boundary energy.

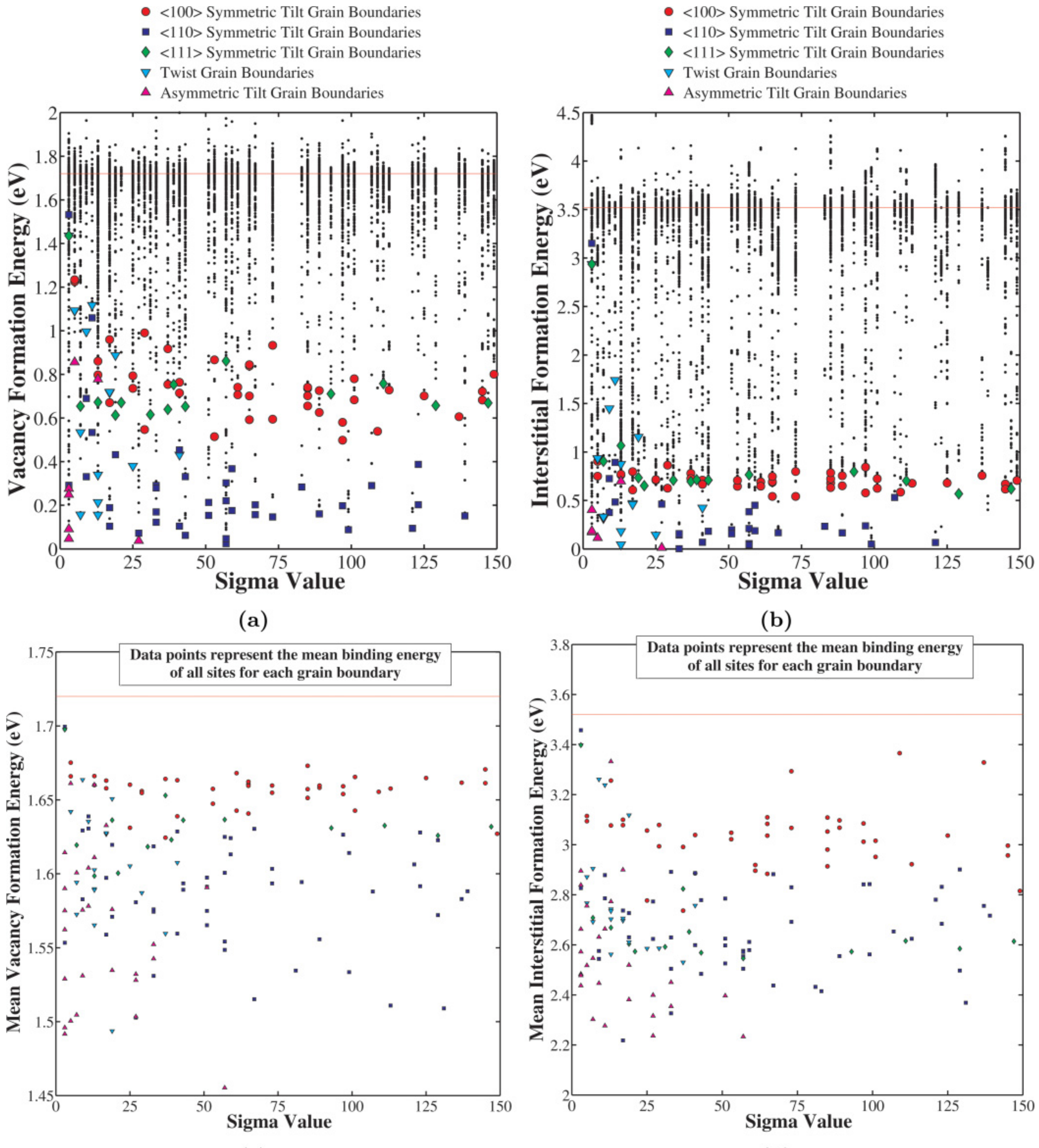

(a) (b) (c) (d)

FIG. 10. (Color online) Vacancy (a) and (b) and interstitial (c) and (d) formation energies as a function of the Σ value for ⟨100⟩, ⟨110⟩, and ⟨111⟩ symmetric tilt grain boundaries. The symbols denote the minimum (a) and (c) and (mean formation energy (b) and (d) for each grain boundary, as in Fig. 8. Aside from a few boundaries, very little trend is observed with respect to Σ value.

The minimum formation energy is plotted as in Fig. 8. The range of grain boundary energies (600–1300 mJ/m^2) is adequate to capture any general trends in the formation energy distributions. First, in Fig. 9, the minimum formation energies for both vacancies and interstitials decrease with increasing grain boundary energy. This trend is highly influenced by both the grain boundary types and special boundaries. As previously observed, the ⟨100⟩ and ⟨111⟩ tilt systems have comparable formation energies, while the ⟨110⟩ tilt grain boundary system has much lower minimum formation energies. In terms of grain boundary energies, the distribution of grain boundary energies in the ⟨100⟩ and ⟨111⟩ systems are lower than in the ⟨110⟩ system in terms of both mean and extreme values; hence, the trend is stronger, but is directly associated with the differences between grain boundaries in different tilt systems. Moreover, this trend is influenced by the much higher vacancy and interstitial formation energies of the Σ3{112} STGB, a twin boundary that also has a very low energy. However, a low energy does not necessarily mean a higher formation energy for point defects. It is anticipated that low-angle grain boundaries (with much lower grain boundary energies than those sampled here) in the ⟨100⟩, ⟨110⟩, and ⟨111⟩ tilt systems should have minimum formation energies similar to the low-angle boundaries probed in this study.

Figures 9(b) and 9(d) show the mean formation energy for vacancies and self-interstitial defects, respectively, within these grain boundaries as a function of the grain boundary energy. As with Fig. 8, additional symmetric/asymmetric tilt and twist grain boundaries were added. There is an obvious trend with respect to the grain boundary energy in these plots. The mean point defect formation energy decreases with increasing grain boundary energy. Moreover, there is some uncertainty in the trend that can be associated with the differences in grain boundary structures, i.e., the multiple potential structures for each grain boundary energy associated with different grain boundary systems or a multiplicity of grain boundary structures can lead to different mean responses.

Last, Fig. 10 shows the vacancy and interstitial formation energy distributions as a function of the Σ designation. For vacancies, the general trend is that the minimum formation energy decreases with increasing Σ designation. For interstitials, there is very little trend, aside from the much higher interstitial formation energy of one boundary: the Σ3{112} STGB. In Fig. 10(b), low-Σ boundaries show the *potential* to have higher minimum vacancy formation energies than general high-Σ grain boundaries; however, this is not always the case (e.g., the Σ3{111} STGB has formation energies similar to general grain boundaries). Moreover, notice that the Σ5 grain boundaries have formation energies higher than general grain boundaries in the case of vacancies, but the formation energies are not so different from general boundaries for interstitials. So not only can the Σ designation of a grain boundary be important, but the defect type also plays a role in whether a particular grain boundary has properties different from general boundaries (i.e., classified as a "special" boundary) or not. Unlike the trends observed with respect to disorientation angle and grain boundary energy for the mean formation energies, the Σ value does not have a strong correlation with either the vacancy or interstitial formation energies [see Figs. 10(b) and 10(d)].

The current results present a slightly different picture than the work of Suzuki and Mishin[39] presented for a few Cu grain boundaries. While the general trend is similar between the two works (i.e., minimum formation energy decreases with increasing grain boundary energy), examining a large number of boundaries in the present work has shown that the grain boundary tilt system plays an important role in the minimum formation energy as well. Moreover, Suzuki and Mishin hypothesize that the minimum formation energy becomes negative at higher grain boundary energies, indicating a maximum possible grain boundary energy in STGBs in Cu. However, the trends within the grain boundary tilt systems shown herein indicate that increasing the grain boundary energy within a tilt system (e.g., ⟨100⟩ STGBs) does not necessarily trend toward more negative formation energies. What is most important is the initial structure of the grain boundary, in particular, whether the boundary is at a minimum energy structure or a near-minimum energy structure. For instance, negative formation energies are associated with grain boundaries in a near-minimum energy structure where removing/adding an atom results in a slightly lower grain boundary energy. This multiplicity of grain boundary structures[52–55] is expected to play a prominent role in the minimum formation energies of point defects.

D. Characterizing the grain boundary site preference, site density, and site strength

Further analysis of these simulations investigates both the grain boundary site preference and methods for characterizing the grain boundary sink strength for point defects in Fe. In doing this analysis, we will also analyze the "absorption" length scale associated with point defect absorption by grain boundaries. The grain boundary site preference can be evaluated by plotting the binding energy for vacancies and self-interstitial atoms against each other for each grain boundary site. This method has been previously applied to ⟨100⟩ symmetric tilt grain boundaries.[79] Figure 11 contains all the binding energies for the 135 minimum energy grain boundaries (≈75 000 simulations). The grain boundary binding energy at a particular site α is calculated by subtracting its formation energy from the bulk formation energy, $E^{\alpha}_{\text{binding}} = E_{\text{f,bulk}} - E^{\alpha}_{\text{f}}$. The line delineates sites where the interstitial binding energy is greater than vacancy binding energies (above the line). The large amount of binding energies above this line indicates that the system energy is decreased more through interstitials occupying grain boundary sites, rather than vacancies. Hence, this plot shows that there is an energetic driving force for interstitials to segregate to grain boundary sites over vacancies. This finding suggests that grain boundaries are, in fact, biased sinks for point defects based on the binding energy alone.

To quantify the grain boundary site preference, Fig. 12 shows the percentage of sites with a greater interstitial binding energy as a function of a binding energy threshold (only sites with a binding energy greater than this threshold are included). For instance, this plot shows that for interstitial binding energies greater than 0.20 eV, 97.5% of grain boundary sites energetically favor an interstitial atom nearby rather than a vacancy. These findings support the interstitial loading-unloading mechanism[23] by showing that it is energetically favorable for interstitials to initially "load" grain boundaries for a wide range of grain boundary types. This is significant for nuclear applications where radiation damage generates these lattice defects and grain boundaries act as sinks for both vacancies and interstitial atoms. Interestingly, the preference for point defect types changes slightly based on the grain boundary system. For instance, there are more favorable sites for vacancies in ⟨110⟩ symmetric tilt grain boundaries and asymmetric tilt grain boundaries than other grain boundary types examined. However, this difference is small, on the order of several percent.

The grain boundary site density and site strength is evaluated for vacancies and interstitial atoms in Fig. 13. In these histograms, a criterion is used to classify potential grain boundary sites based on whether the binding energy for a particular site is greater than 0.05 eV (i.e., 0.05 eV lower formation energy than the bulk formation energy). Hence, this criterion eliminates the influence of atoms in the bulk lattice surrounding the boundary. The grain boundary site density is then calculated by dividing the number of potential sites by the grain boundary area. Figures 13(a) and 13(b) show the resulting grain boundary site density distributions for all grain boundaries in this study. The associated mean, standard deviation, and maximum grain boundary site density is also given in the histogram. The site density for self-interstitial atoms is ≈80% higher than for vacancies. Figures 13(c) and 13(d) show the distributions of the grain boundary site strength, as measured by the mean binding energy of all potential sites based on the same criterion. The mean binding energy for vacancies is 0.45 eV, while the mean binding energy for interstitials is 1.75 eV (≈300% higher). Hence, both the number of grain boundary sites as well as the mean grain boundary site strength are much greater for interstitials than for vacancies. The breakdown of the various grain boundary types is also displayed in this stacked histogram, showing the site density and site strength variability for each grain boundary type. In general, the different grain boundary types are dispersed over a wide range of site density and site strength values. In some cases, there are small differences between the grain boundary systems. For example, in the grain boundary site strength histograms, the ⟨100⟩ STGBs tend to have lower binding energies than the other grain boundary systems. These data are also summarized in Tables I and II, which list the point defect data for individual low-Σ symmetric tilt grain boundaries ($\Sigma \leqslant 13$) as well as the mean statistics for high-Σ symmetric tilt grain boundaries ($\Sigma > 13$), twist boundaries, and asymmetric tilt boundaries. The following study can provide guidance as to which grain boundaries are different from or representative of more general high-Σ grain boundaries.

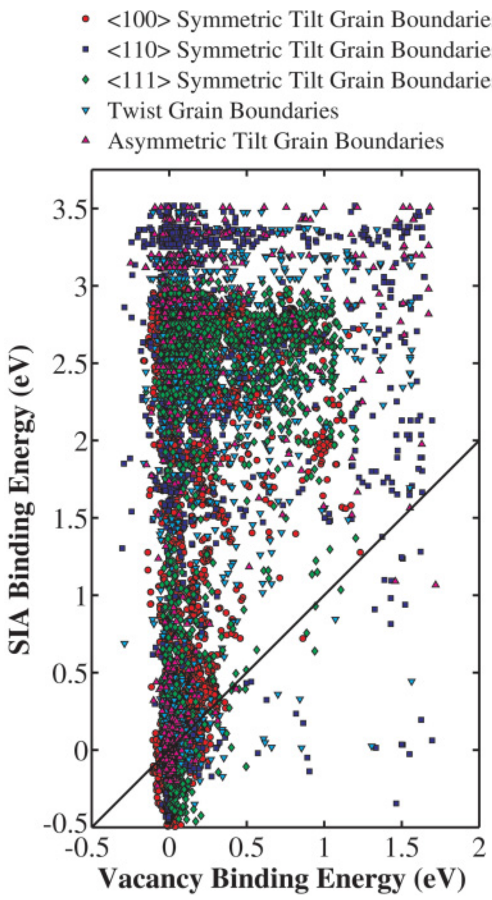

FIG. 11. (Color online) Grain boundary site preference is shown by plotting the vacancy binding energy against the corresponding interstitial binding energy for each site in this study. The line represents equal binding energies for vacancies and interstitial atoms. Similar to prior results in the ⟨100⟩ system,[79] albeit with a larger sampling of grain boundaries, there is an energetic preference for binding of interstitials to grain boundaries over vacancies.

E. Quantifying the absorption length scale of point defects by grain boundaries

There is an inherent length scale associated with point defect absorption to grain boundaries that is influenced by both the defect type and the grain boundary character. In addition to the energetics, the length scales associated with the grain boundary interface are also important for higher scale models that may require details of the sharp or diffuse nature of grain boundaries and their interaction with point defects. Figure 14 shows how the mean vacancy and interstitial binding energies decrease as a function of distance from the

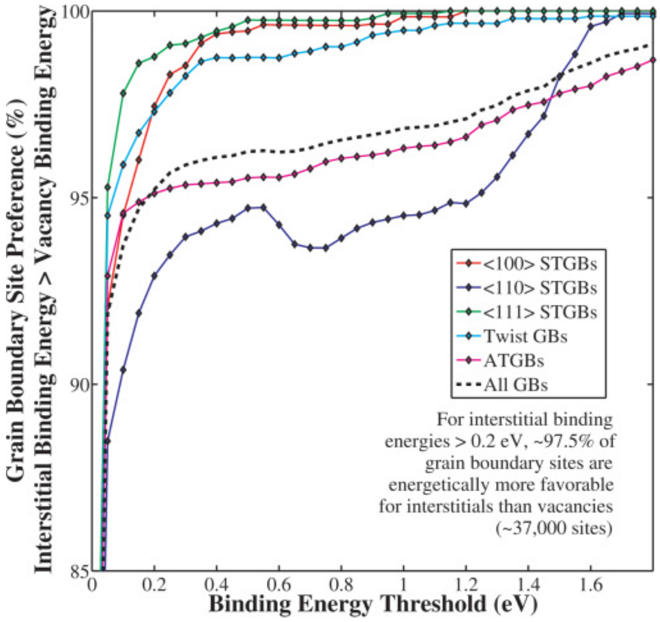

For interstitial binding energies > 0.2 eV, ~97.5% of grain boundary sites are energetically more favorable for interstitials than vacancies (~37,000 sites)

FIG. 12. (Color online) The percentage of grain boundary sites that prefer an interstitial to a vacancy as a function of the binding energy threshold given. While there is a difference between the different grain boundary systems, overall grain boundary sites have a preference for interstitial atoms over vacancies in terms of binding energies.

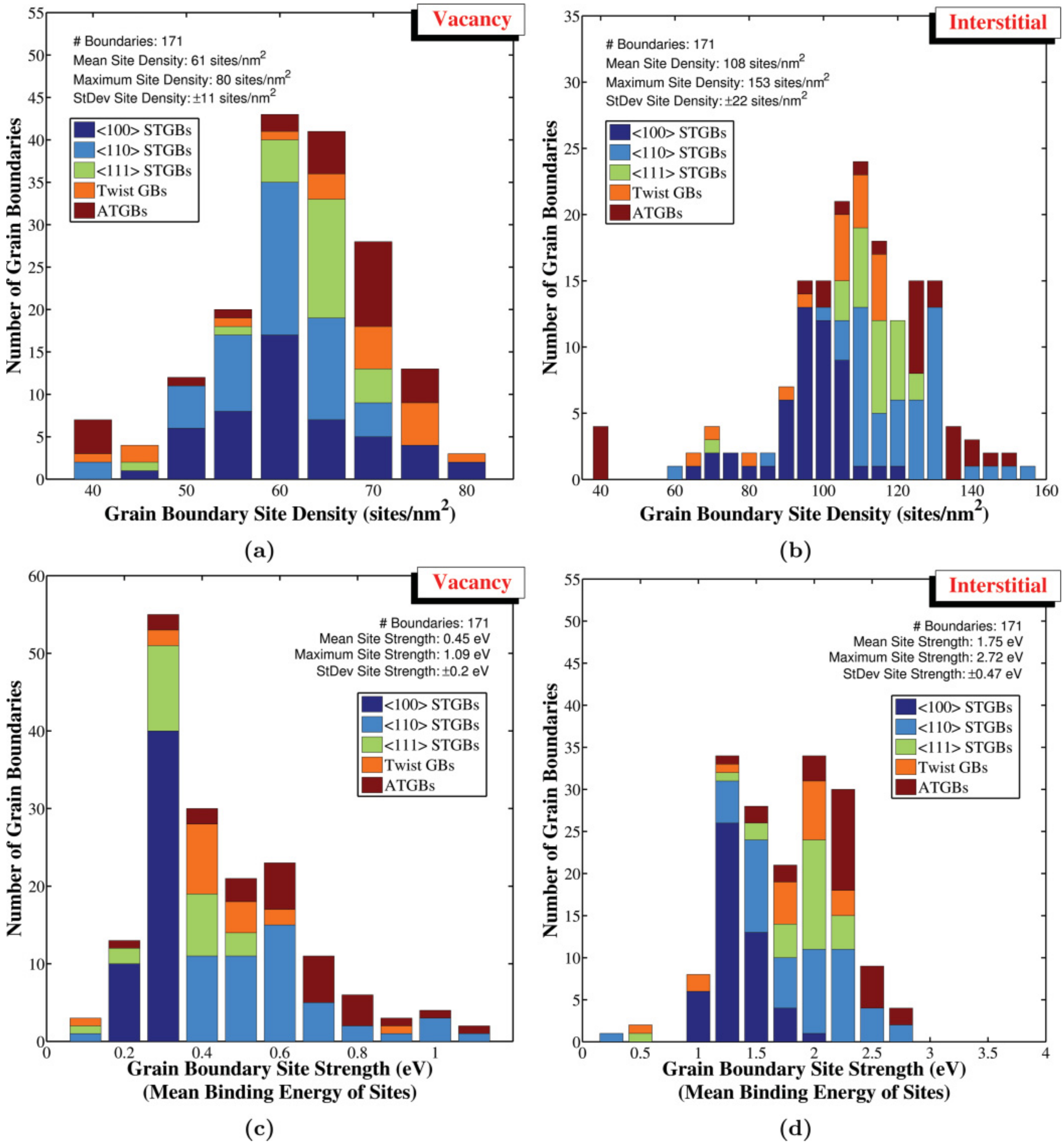

FIG. 13. (Color online) Histograms of the grain boundary (a) and (b) site density and (c) and (d) site strength for (a) and (c) vacancies and (b) and (d) interstitials. Grain boundary sites were classified according to a criterion that required the binding energy to be greater than 0.05 eV, distinguishing atoms in the bulk lattice from those in the grain boundary.

boundary. For this plot, the binding energies are calculated using bins that are 2 Å wide. As shown in the inset histogram, the mean binding energy for each boundary is calculated for each bin. The plotted mean binding energy for each bin is calculated by taking the mean of the corresponding histogram; this process guarantees that each boundary is equally weighted. The error bars are equal to one standard deviation from the mean vacancy and interstitial binding energies for each bin. This plot shows that the interstitial binding energies are much greater than vacancy binding energies, similar to previous results. The mean binding energy tends to be greatest near the grain boundary center and decreases as the distance from the grain boundary center increases. Moreover, the mean vacancy binding energy approaches 0 eV at 6–7 Å, whereas the mean

TABLE I. Summary of point defect statistics for low-Σ symmetric tilt grain boundaries ($\Sigma \leqslant 13$), including grain boundary energy (γ_{GB}), grain boundary area (A_{GB}), site density (ρ), and minimum formation energy ($E_{\mathrm{f,min}}$), and mean binding energy ($E_{\mathrm{b,mean}}$) of the point defects.

			Vacancy			Interstitial		
Grain boundary	γ_{GB} (mJ/m^2)	A_{GB} (nm^2)	ρ (site/nm^2)	$E_{\mathrm{f,min}}$ (eV)	$E_{\mathrm{b,mean}}$ (eV)	ρ (site/nm^2)	$E_{\mathrm{f,min}}$ (eV)	$E_{\mathrm{b,mean}}$ (eV)
$\Sigma3\{112\}\langle110\rangle\theta = 60.00^\circ$	262	0.20	40	1.53	0.13	60	3.15	0.25
$\Sigma3\{111\}\langle110\rangle\theta = 60.00^\circ$	1297	0.28	42	0.29	1.03	149	−0.08	1.34
$\Sigma3\{011\}\langle111\rangle\theta = 60.00^\circ$	309	0.35	46	1.44	0.13	69	2.94	0.45
$\Sigma5\{012\}\langle100\rangle\theta = 36.87^\circ$	1096	0.18	60	1.23	0.26	88	0.75	1.29
$\Sigma5\{013\}\langle100\rangle\theta = 36.87^\circ$	987	0.26	47	1.23	0.27	70	0.90	1.52
$\Sigma7\{123\}\langle111\rangle\theta = 21.79^\circ$	1047	0.92	59	0.65	0.44	116	0.90	1.86
$\Sigma9\{114\}\langle110\rangle\theta = 38.94^\circ$	1146	0.35	52	0.69	0.46	104	0.73	2.31
$\Sigma9\{221\}\langle110\rangle\theta = 38.94^\circ$	1282	0.49	65	0.33	0.55	106	0.38	2.37
$\Sigma11\{332\}\langle110\rangle\theta = 50.48^\circ$	1018	0.38	52	1.06	0.42	84	0.89	1.97
$\Sigma11\{113\}\langle110\rangle\theta = 50.48^\circ$	1097	0.54	59	0.53	0.41	100	0.48	1.88
$\Sigma13a\{023\}\langle100\rangle\theta = 22.62^\circ$	1094	0.29	68	0.80	0.24	95	0.76	1.08
$\Sigma13a\{015\}\langle100\rangle\theta = 22.62^\circ$	992	0.42	58	0.86	0.26	96	0.77	1.20
$\Sigma13b\{134\}\langle111\rangle\theta = 32.20^\circ$	1107	1.25	58	0.67	0.55	109	1.07	2.04

interstitial binding energy approaches 0 eV at 10–11 Å. The mean difference in terms of the absorption length scale of grain boundaries is on the order of 4 Å, which is over a full lattice unit difference ($a_0 = 2.8553$ Å) in terms of the affected length scale. A similar trend is observed for the maximum binding energies, i.e., the maximum binding energy approaches 0 eV at a greater distance for interstitials than for vacancies (not shown). This supports the finding that grain boundaries tend to have a much larger length scale for absorption of interstitial atoms over vacancies as well.

How the grain boundary character affects the energies and point defect absorption length scales was also investigated. Figure 15 shows how the mean vacancy and interstitial binding energies decrease as a function of distance for the different grain boundary systems examined herein. This plot is similar to Fig. 15 with bins that are 2 Å wide. First, in both plots, the ⟨100⟩ symmetric tilt boundaries tend to have the lowest binding energy curves, while the asymmetric boundaries sampled tended to have the highest binding energy curves. The binding energy curves for the different systems tend to follow similar relationships with respect to distance from the grain boundary center, with some curves having slightly lower binding energies in the 0 Å bin than bins a few Å from the grain boundary center. These results agree with those of Wen *et al.*,[109] who used molecular dynamics to sample vacancy formation and diffusion energies in both $\Sigma5$ symmetric tilt grain boundaries for iron and found that vacancies located within 8–10 layers from the grain boundary center would tend to favorably migrate and aggregate to the second layer (i.e., just adjacent to the grain boundary center). Again, the increase in mean binding energy for the 1 Å bins in a few grain boundary systems suggests that this behavior extends to more boundaries than just the $\Sigma5$ sampled by Wen and colleagues. On another note, these plots show that the absorption length scale is affected by the grain boundary character. While the mean vacancy binding energies approach 0 eV at very similar distances (≈7 Å), the mean interstitial binding energies approach 0 eV from 8 Å (⟨100⟩ STGBs) to 11 Å (ATGBs). Clearly, both the mean point defect energies and the absorption length scale is affected by grain boundary character. However, as Fig. 14 shows, the type of point defect is even more important in terms of characterizing the strength of the grain boundary as a sink for point defects.

The following study has systematically investigated the effect of point defect absorption by grain boundaries, in particular, paying attention to the vast array of grain boundary systems. While the results for a larger number of grain boundaries and more complex grain boundaries, i.e., mixed tilt twist, could also be added or another Fe interatomic potential could be used, the trends calculated within the present study provide both qualitative and quantitative understanding of grain boundaries acting as sinks for point defects. There

TABLE II. Summary of mean point defect statistics for general boundaries in different systems.

			Vacancy			Interstitial		
Grain boundary	γ_{GB} (mJ/m^2)	A_{GB} (nm^2)	ρ (site/nm^2)	$E_{\mathrm{f,min}}$ (eV)	$E_{\mathrm{b,mean}}$ (eV)	ρ (site/nm^2)	$E_{\mathrm{f,min}}$ (eV)	$E_{\mathrm{b,mean}}$ (eV)
⟨100⟩ STGBs $\Sigma > 13$	988	0.83	62	0.72	0.27	96	0.68	1.36
⟨110⟩ STGBs $\Sigma > 13$	1136	1.02	60	0.19	0.60	122	−0.15	1.91
⟨111⟩ STGBs $\Sigma > 13$	974	1.62	64	0.69	0.35	115	0.69	1.92
All Twist GBs	1083	2.15	65	0.48	0.44	102	0.64	1.73
All ATGBs	1477	8.37	59	−1.05	0.63	109	−1.59	2.17

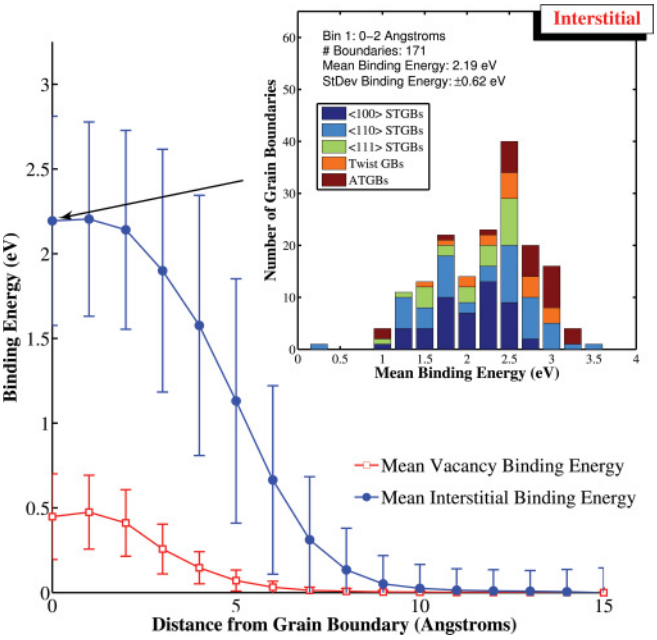

FIG. 14. (Color online) Evolution of the vacancy and interstitial mean binding energies as a function of the distance from the grain boundary center. The mean binding energies for each 2 Å bin are calculated from the binding energy distributions for the sampled grain boundaries (inset histogram). Grain boundaries tend to have both a larger binding energy and absorption length scale for interstitial defects over vacancies.

are still a number of avenues for future work, e.g., the influence of temperature/entropy,[39–41] the influence of strain, the multiplicity of grain boundary structures,[52–55] uncertainty in results due to the interatomic potential development process,[110,111] or even data mining/informatics approaches for creating knowledge from the present simulations,[112–116] etc. We leave these avenues for future studies. Last, the sheer volume of information stemming from such an approach can enable higher scale models to accept relationships such as that shown in Fig. 14 while also quantifying the uncertainty due to grain boundary character and interfacial length scales in polycrystals.

IV. CONCLUSIONS

This research investigated how grain boundary character influences the formation of vacancies and interstitials in grain boundaries for bcc Fe. Molecular statics simulations were used to generate a grain boundary structure database that contained ⟨100⟩, ⟨110⟩, and ⟨111⟩ symmetric tilt-grain, twist-grain, and asymmetric tilt-grain boundaries. Then, simulations were used to calculate vacancy and self-interstitial atom formation energies at all potential grain boundary sites within 15 Å of the boundary. The present results provide detailed information about the interaction energies of vacancies and interstitial atoms with symmetric tilt grain boundaries in iron. The following conclusions can be drawn from this work.

(1) The local atomic structure and spatial location within the boundary affects the magnitude of the formation energies for vacancies and self-interstitial atoms (see Fig. 5). In general, grain boundary sites have much lower formation energies for vacancies and interstitials than in the bulk. However, for both vacancies and interstitials, there are some sites near or within the boundary that exhibit higher formation energies than in

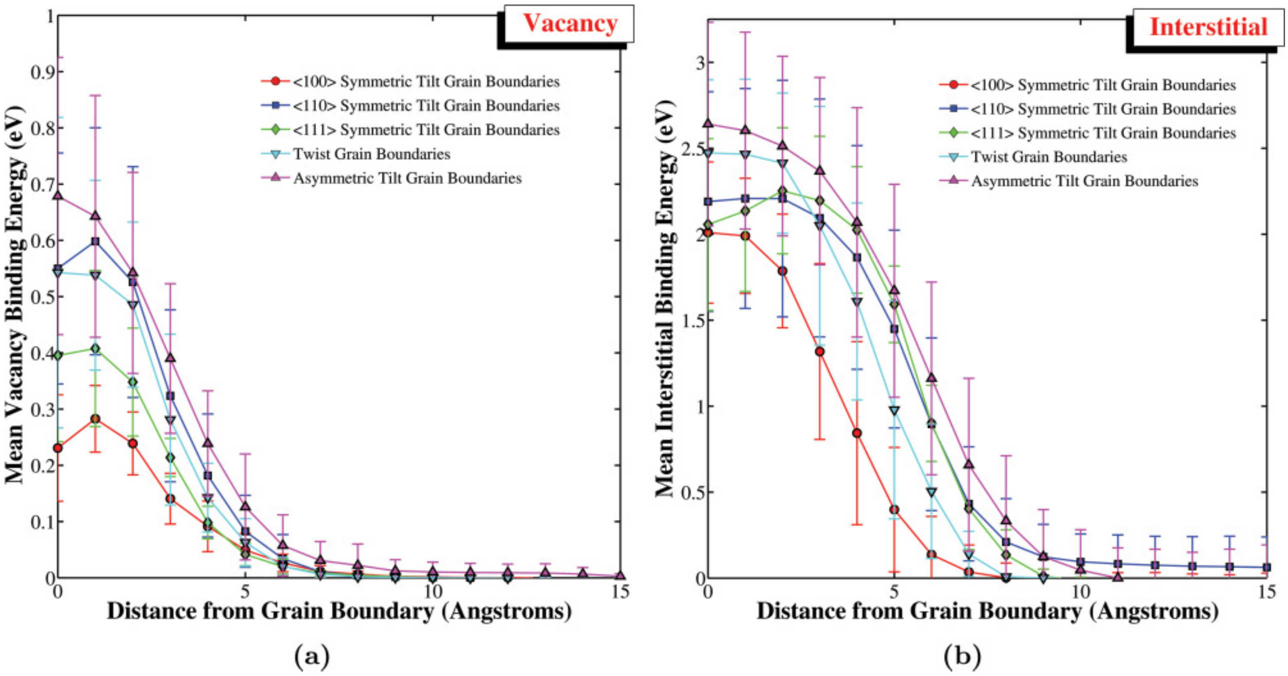

FIG. 15. (Color online) Evolution of the (a) vacancy and (b) interstitial mean binding energies as a function of the distance from the grain boundary center. The mean binding energies for each 2 Å bin are calculated from the binding energy distributions for the different grain boundary systems displayed. The binding energy curves and absorption length scales for both interstitial defects and vacancies are sensitive to the type of grain boundary system.

the bulk. Moreover, low-angle boundaries were found to be an effective sink for vacancies and interstitial atoms along planes adjacent to grain boundary dislocations (see Fig. 6), in some cases extending several lattice units from the dislocation core. The regions between dislocations have formation energies similar to bulk values, as expected. In general, the interaction regions of both low- and high-angle boundaries were larger for interstitial atoms than for vacancies. Also, for both low- and high-angle boundaries, interstitials tended to have lower formation energies relative to the bulk formation energy.

(2) The distance from the center of the grain boundary affects the formation energies for vacancies and interstitials (see Fig. 7). For vacancies, the lowest and highest formation energies are typically found near the center of the grain boundary. For interstitials, the formation energies are similar within the grain boundary region with a band of minimum formation energies that extends over 5 Å from the grain boundary center for the ⟨100⟩ tilt system.

(3) The grain boundary character was found to affect the point defect formation energies as well (see Figs. 8–10). The ⟨110⟩ symmetric tilt grain boundaries tended to have lower minimum vacancy and interstitial formation energies than the ⟨100⟩ and ⟨111⟩ tilt boundaries. Moreover, the $\Sigma3\{112\}$, $\Sigma5\{310\}$, $\Sigma5\{210\}$, and the $\Sigma11\{332\}$ boundaries have much higher vacancy formation energies than other boundaries in this study. The $\Sigma3\{112\}$ twin boundary has much higher interstitial formation energies than other boundaries as well. The trends with respect to disorientation angle, grain boundary energy, and Σ value were analyzed by comparing with both the minimum and mean point defect formation energies for each boundary. In general, the minimum and mean point defect formation energies decreased with increasing disorientation angle, grain boundary energy, and Σ value, with the strongest trend being the mean formation energy and grain boundary energy [see Figs. 9(b) and 9(d)]. The trend with Σ value was mainly due to a few of the aforementioned special boundaries (also listed in Table I).

(4) Grain boundaries in the α-iron system are biased sinks for point defects based on the binding energy of grain boundary sites. The majority of grain boundary sites have a larger binding energy for interstitials than vacancies (see Fig. 11). Thus there is an energetic driving force for self-interstitial atoms to occupy most grain boundary sites over vacancies. For binding energies greater than 0.2 eV, more than 97% of sites prefer interstitials (see Fig. 12).

(5) Grain boundary site metrics were calculated to characterize the sink strength of the grain boundary-point defect interaction (see Fig. 13). The mean grain boundary site density and site strength are ≈80% and ≈300% greater for interstitials than for vacancies, respectively.

(6) There is an inherent length scale associated with point defect absorption by grain boundaries that is influenced by both the defect type and the grain boundary character. For instance, the mean vacancy binding energy approaches 0 eV at 6–7 Å, whereas the mean interstitial binding energy approaches 0 eV at 10–11 Å—over a full lattice unit difference in terms of the affected "absorption" length scale. Moreover, there is a large degree of variability in the binding energies and the inherent length scale of absorption associated with the grain boundary character (see Figs. 14 and 15). Atomistic simulations of this nature may ultimately help our understanding of how interface structure affects point defect and element segregation to grain boundaries in polycrystalline materials.

ACKNOWLEDGMENTS

The authors would like to thank the reviewers for their insightful comments during the review process. This work was funded by the U.S. Department of Energy's Nuclear Energy Advanced Modeling and Simulation (NEAMS) program at Pacific Northwest National Laboratory. PNNL is operated by Battelle Memorial Institute for the U.S. Department of Energy under contract No. DE-AC05-76RL01830. K.N.S. would like to acknowledge the support by the Office of Naval Research under contract No. N00014-09-1-0661.

---

*mtschopp@cavs.msstate.edu

[1] G. S. Was, *Fundamentals of Radiation Materials Science: Metals and Alloys*, 1st ed. (Springer, New York, Berlin, Heidelberg, 2007).

[2] G. Ackland, Science **327**, 1587 (2010).

[3] T. R. Allen, J. T. Busby, G. S. Was, and E. A. Kenik, J. Nucl. Mater. **255**, 44 (1998).

[4] S. M. Bruemmer, E. P. Simonen, P. M. Scott, P. L. Andresen, G. S. Was, and J. L. Nelson, J. Nucl. Mater. **274**, 299 (1999).

[5] D. L. Damcott, T. Allen, and G. S. Was, J. Nucl. Mater. **225**, 97 (1995).

[6] T. S. Duh, J. J. Kai, F. R. Chen, and L. H. Wang, J. Nucl. Mater. **258–263**, 2064 (1998).

[7] T. S. Duh, J. J. Kai, and F. R. Chen, J. Nucl. Mater. **283–287**, 198 (2000).

[8] T. S. Duh, J. J. Kai, F. R. Chen, and L. H. Wang, J. Nucl. Mater. **294**, 267 (2001).

[9] A. Etienne, B. Radiguet, N. J. Cunningham, G. R. Odette, and P. Pareige, J. Nucl. Mater. **406**, 244 (2010).

[10] Z. Jiao and G. S. Was, Acta Mater. **59**, 1220 (2011).

[11] Z. Lu, R. G. Faulkner, G. Was, and B. D. Wirth, Scr. Mater. **58**, 878 (2008).

[12] G. S. Was, J. P. Wharry, B. Frisbie, B. D. Wirth, D. Morgan, J. D. Tucker, and T. R. Allen, J. Nucl. Mater. **411**, 41 (2011).

[13] J. P. Wharry, Z. Jiao, V. Shankar, J. T. Busby, and G. S. Was, J. Nucl. Mater. **417**, 140 (2011).

[14] S. Watanabe, Y. Takamatsu, N. Sakaguchi, and H. Takahashi, J. Nucl. Mater. **283–287**, 152 (2000).

[15] M. Dollar and H. Gleiter, Scr. Metall. **19**, 481 (1985).

[16] T. Watanabe, Res Mech. **11**, 47 (1984).

[17] G. S. Rohrer, D. M. Saylor, B. E. Dasher, B. L. Adams, A. D. Rollett, and P. Wynblatt, Zeitschrift fuer Metallkunde/Mater. Res. and Adv. Tech. **95**, 197 (2004).

[18] G. S. Rohrer, V. Randle, C.-S. Kim, and Y. Hu, Acta Mater. **54**, 4489 (2006).

[19] D. M. Saylor, A. Morawiec, and G. S. Rohrer, Acta Mater. **51**, 3663 (2003).

[20] D. M. Saylor, B. S. E. Dasher, A. D. Rollett, and G. S. Rohrer, Acta Mater. **52**, 3649 (2004).

[21] C.-S. Kim, Y. Hu, G. S. Rohrer, and V. Randle, Scr. Mater. **52**, 633 (2005).

[22] M. Sekine, N. Sakaguchi, M. Endo, H. Kinoshita, S. Watanabe, H. Kokawa, S. Yamashita, Y. Yano, and M. Kawai, J. Nucl. Mater. **414**, 232 (2011).

[23] X. Bai, A. F. Voter, R. G. Hoagland, M. Nastasi, and B. P. Uberuaga, Science **327**, 1631 (2010).

[24] M. Samaras, P. M. Derlet, H. Van Swygenhoven, and M. Victoria, J. Nucl. Mater. **351**, 47 (2006).

[25] M. Samaras, P. M. Derlet, H. Van Swygenhoven, and M. Victoria, Nucl. Instrum. Methods Phys. Res., Sect. B **202**, 51 (2003).

[26] M. Samaras, P. M. Derlet, H. Van Swygenhoven, and M. Victoria, J. Nucl. Mater. **323**, 213 (2003).

[27] M. Samaras, P. M. Derlet, H. Van Swygenhoven, and M. Victoria, Philos. Mag. **83**, 3599 (2003).

[28] P. C. Millett, D. Wolf, T. Desai, and V. Yamakov, Appl. Phys. Lett. **93**, 161902 (2008).

[29] P. C. Millett, D. S. Aidhy, T. Desai, S. R. Phillpot, and D. Wolf, Int. J. Mater. Res. **100**, 550 (2009).

[30] N. Gao, M. Samaras, and H. Van Swygenhoven, J. Nucl. Mater. **400**, 240 (2010).

[31] F. J. Perez-Perez and R. Smith, Nucl. Instrum. Methods Phys. Res., Sect. B **153**, 136 (1999).

[32] F. J. Perez-Perez and R. Smith, Nucl. Instrum. Methods Phys. Res., Sect. B **180**, 322 (2001).

[33] A. Misra, M. J. Demkowicz, J. Wang, and R. G. Hoagland, JOM **60**, 39 (2008).

[34] A. Misra, M. J. Demkowicz, X. Zhang, and R. G. Hoagland, JOM **59**, 62 (2007).

[35] H. L. Heinisch, F. Gao, and R. J. Kurtz, J. Nucl. Mater. **329–333**, 924 (2004).

[36] T. Kwok, P. S. Ho, S. Yip, R. W. Balluffi, P. D. Bristowe, and A. Brokman, Phys. Rev. Lett. **47**, 1148 (1981).

[37] T. Kwok, P. S. Ho, and S. Yip, Phys. Rev. B **29**, 5354 (1984).

[38] T. Kwok, P. S. Ho, and S. Yip, Phys. Rev. B **29**, 5363 (1984).

[39] A. Suzuki and Y. Mishin, Interf. Sci. **11**, 131 (2003).

[40] A. Suzuki and Y. Mishin, J. Mater. Sci. **40**, 3155 (2005).

[41] A. Suzuki and Y. Mishin, Interf. Sci. **11**, 425 (2003).

[42] M. J. Demkowicz, O. Anderoglu, X. Zhang, and A. Misra, J. Mater. Res. **26**, 1666 (2011).

[43] C. Forwood and L. Clarebrough, *Electron Microscopy of Interfaces in Metals and Alloys* (IOP, Bristol, UK, 1991).

[44] C. T. Forwood and L. M. Clarebrough, Philos. Mag. A **53**, 863 (1986).

[45] O. H. Duparc, S. Poulat, A. Larere, J. Thibault, and L. Priester, Philos. Mag. A **80**, 853 (2000).

[46] O. H. Duparc, J.-P. Couziniè, J. Thibault-Pènisson, S. Lartigue-Korinek, B. Dècamps, and L. Priester, Acta Mater. **55**, 1791 (2007).

[47] A. P. Sutton and R. W. Balluffi, *Interfaces in Crystalline Materials* (Oxford University Press, USA, 1997).

[48] D. Wolf and S. Yip, *Materials Interfaces: Atomic-level Structure and Properties*, 1st ed. (Chapman and Hall, London, UK, 1992).

[49] A. P. Sutton and V. Vitek, Philos. Trans. R. Soc. London A **309**, 1 (1983).

[50] A. P. Sutton and V. Vitek, Philos. Trans. R. Soc. London A **309**, 37 (1983).

[51] A. P. Sutton and V. Vitek, Philos. Trans. R. Soc. London A **309**, 55 (1983).

[52] G.-J. Wang and V. Vitek, Acta Metall. **34**, 951 (1986).

[53] V. Vitek, A. P. Sutton, G. J. Wang, and D. Schwartz, Scr. Metall. **17**, 183 (1983).

[54] G. J. Wang, A. P. Sutton, and V. Vitek, Acta Metall. **32**, 1093 (1984).

[55] V. Vitek, Y. Minonishi, and G. J. Wang, J. Phys. **46**, C4 (1985).

[56] The importance of which was demonstrated in D. Wolf, Scr. Metall. **23**, 1713 (1989).

[57] D. Wolf, Scr. Metall. **23**, 1913 (1989).

[58] D. Wolf, Acta Metall. Mater. **38**, 791 (1990).

[59] D. Wolf, Acta Metall. Mater. **38**, 781 (1990).

[60] E. A. Holm, D. L. Olmsted, and S. M. Foiles, Scr. Mater. **63**, 905 (2010).

[61] M. A. Tschopp, G. J. Tucker, and D. L. McDowell, Acta Mater. **55**, 3959 (2007).

[62] M. A. Tschopp, D. E. Spearot, and D. L. McDowell, Modell. Simul. Mater. Sci. Eng. **15**, 693 (2007).

[63] M. A. Tschopp and D. L. McDowell, Philos. Mag. **87**, 3871 (2007).

[64] M. A. Tschopp and D. L. McDowell, Philos. Mag. **87**, 3147 (2007).

[65] M. A. Tschopp and D. L. McDowell, J. Mater. Sci. **42**, 7806 (2007).

[66] D. L. Olmsted, E. Holm, and S. Foiles, Acta Mater. **57**, 3704 (2009).

[67] D. L. Olmsted, S. Foiles, and E. Holm, Acta Mater. **57**, 3694 (2009).

[68] D. E. Spearot, K. I. Jacob, and D. L. McDowell, Acta Mater. **53**, 3579 (2005).

[69] D. E. Spearot, M. A. Tschopp, K. I. Jacob, and D. L. McDowell, Acta Mater. **55**, 705 (2007).

[70] D. E. Spearot, M. A. Tschopp, and D. L. McDowell, Scr. Mater. **60**, 675 (2009).

[71] M. A. Tschopp, D. E. Spearot, and D. L. McDowell, *Influence of Grain Boundary Structure on Dislocation Nucleation in FCC Metals* Vol. 14 (Elsevier, Oxford, UK, 2008), Chap. 82, pp. 43–139.

[72] M. A. Tschopp, G. J. Tucker, and D. L. McDowell, Comput. Mater. Sci. **44**, 351 (2008).

[73] M. A. Tschopp and D. L. McDowell, Scr. Mater. **58**, 299 (2008).

[74] M. A. Tschopp and D. L. McDowell, Int. J. Plast. **24**, 191 (2008).

[75] G. J. Tucker, M. A. Tschopp, and D. L. McDowell, Acta Mater. **58**, 6464 (2010).

[76] M. P. Dewald and W. A. Curtin, Modell. Simul. Mater. Sci. Eng. **15**, S193 (2007).

[77] M. P. Dewald and W. A. Curtin, Philos. Mag. **87**, 4615 (2007).

[78] M. P. Dewald and W. A. Curtin, Modell. Simul. Mater. Sci. Eng. **19**, 055002 (2011).

[79] M. A. Tschopp, M. F. Horstemeyer, F. Gao, X. Sun, and M. Khaleel, Scr. Mater. **64**, 908 (2011).

[80] S. Plimpton, J. Comput. Phys. **117**, 1 (1995).

[81] J. D. Rittner, D. N. Seidman, and K. L. Merkle, Phys. Rev. B **53**, R4241 (1996).

[82] M. I. Mendelev, S. Han, D. J. Srolovitz, G. J. Ackland, D. Y. Sun, and M. Asta, Philos. Mag. **83**, 3977 (2003).

[83] NIST interatomic potential website: [http://www.ctcms.nist.gov/potentials/index.html].

[84] M. S. Daw and M. I. Baskes, Phys. Rev. B **29**, 6443 (1984).

[85] M. S. Daw and M. I. Baskes, Phys. Rev. Lett. **50**, 1285 (1983).

[86] L. Malerba, M. C. Marinica, N. Anento, C. Björkas, H. Nguyen, C. Domain, F. Djurabekova, P. Olsson, K. Nordlund, A. Serra, D. Terentyev, F. Willaime, and C. S. Becquart, J. Nucl. Mater. **406**, 19 (2010).

[87] J. D. Rittner and D. N. Seidman, Phys. Rev. B **54**, 6999 (1996).

[88] W. T. Read and W. Shockley, Phys. Rev. **78**, 275 (1950).

[89] F. Humphreys and M. Hatherly, *Recrystallization and Related Annealing Phenomena* (Pergamon, Oxford, UK, 1995).

[90] G. H. Bishop and B. Chalmers, Scr. Metall. **2**, 133 (1968).

[91] G. H. Bishop and B. Chalmers, Philos. Mag. **24**, 515 (1971).

[92] A. P. Sutton, Philos. Mag. **59**, 53 (1989).

[93] M. J. Demkowicz, J. Wang, and R. G. Hoagland, *Interfaces Between Dissimilar Crystalline Solids* in Dislocations in Solids Vol. 14 (Elsevier, Oxford, UK, 2008), Chap. 83.

[94] M. J. Demkowicz, R. G. Hoagland, and J. P. Hirth, Phys. Rev. Lett. **100**, 136102 (2008).

[95] M. J. Demkowicz, P. Bellon, and B. D. Wirth, MRS Bull. **35**, 992 (2010).

[96] K. Ingle and A. Crocker, Acta Metall. **26**, 1461 (1978).

[97] E. Clouet, Acta Mater. **54**, 3543 (2006).

[98] T. T. Lau, X. Lin, S. Yip, and K. J. V. Vliet, Scr. Mater. **60**, 399 (2009).

[99] E. Kuramoto, K. Ohsawa, and T. Tsutsumi, J. Nucl. Mater. **283–287**, 778 (2000).

[100] K. Sato, T. Yoshiie, T. Ishizaki, and Q. Xu, J. Nucl. Mater. **329–333**, 929 (2004).

[101] M. Doyama, Y. Kogure, and T. Nozaki, Nucl. Instrum. Method. Phys. Res., Sect. B **255**, 85 (2007).

[102] Y. X. Wang, Q. Xu, T. Yoshiie, and Z. Y. Pan, J. Nucl. Mater. **376**, 133 (2008).

[103] H. L. Heinisch, F. Gao, and R. J. Kurtz, J. Nucl. Mater. **367-370**, 311 (2007).

[104] H. L. Heinisch, F. Gao, R. J. Kurtz, and E. Le, J. Nucl. Mater. **351**, 141 (2006).

[105] V. Y. Gertsman, A. A. Nazarov, A. E. Romanov, R. Z. Valiev, and V. I. Vladimirov, Philos. Mag. A **59**, 1113 (1989).

[106] A. A. Nazarov, O. A. Shenderova, and D. W. Brenner, Mater. Sci. Eng. A **281**, 148 (2000).

[107] O. A. Shenderova, D. W. Brenner, A. A. Nazarov, A. E. Romanov, and L. H. Yang, Phys. Rev. B **57**, 3181 (1998).

[108] O. A. Shenderova, D. W. Brenner, and L. H. Yang, Phys. Rev. B **60**, 7043 (1999).

[109] Y.-N. Wen, Y. Zhang, J.-M. Zhang, and K.-W. Xu, Comput. Mater. Sci. **50**, 2087 (2011).

[110] M. A. Tschopp, K. N. Solanki, M. I. Baskes, F. Gao, X. Sun, and M. F. Horstemeyer, J. Nucl. Mater. (in press), doi: 10.1016/j.jnucmat.2011.08.003.

[111] M. A. Tschopp, K. N. Solanki, and M. F. Horstemeyer, *Tools Developed and Needed to Realize the Vision of Integrated Computational Materials Engineering* (ASM International, Ohio, USA, 2011).

[112] K. Rajan, Materials Today **8**, 38 (2005).

[113] K. Rajan and P. Mendez, Stat. Anal. Data Min. **1**, 286 (2009).

[114] K. Rajan, Annu. Rev. Mater. Res. **38**, 299 (2008).

[115] S. Broderick, C. Suh, J. Nowers, B. Vogel, S. Mallapragada, B. Narasimhan, and K. Rajan, JOM **60**, 56 (2008).

[116] S. R. Broderick, H. Aourag, and K. Rajan, Physica B **406**, 2055 (2011).